UNIVERSITY OF CALGARY

Process Tomography of Photon Creation and Annihilation Operators

by

Ranjeet Kumar

A THESIS
SUBMITTED TO THE FACULTY OF GRADUATE STUDIES
IN PARTIAL FULFILLMENT OF THE REQUIREMENTS FOR THE
DEGREE OF MASTER OF SCIENCE

DEPARTMENT OF PHYSICS AND ASTRONOMY
AND
INSTITUTE FOR QUANTUM INFORMATION SCIENCE

CALGARY, ALBERTA
June, 2012

UNIVERSITY OF CALGARY

FACULTY OF GRADUATE STUDIES

The undersigned certify that they have read, and recommend to the Faculty of Graduate Studies for acceptance, a thesis entitled "Process Tomography of Photon Creation and Annihilation Operators" submitted by Ranjeet Kumar in partial fulfillment of the requirements for the degree of MASTER OF SCIENCE.

Supervisor, Dr. Alexander I. Lvovsky
Department of Physics and Astronomy

Dr. Christoph Simon
Department of Physics and Astronomy

Dr. Paul Barclay
Department of Physics and Astronomy

Dr. John S. Nielsen
Department of Electrical Engineering

Date

Abstract

The photon creation and annihilation operators are cornerstones of the quantum description of the electromagnetic field. They signify the isomorphism of the optical Hilbert space to that of the harmonic oscillator and the bosonic nature of photons. We perform complete experimental characterization (quantum process tomography) of these operators. By measuring, via homodyne detection, their effect on coherent states, we obtain their process tensor in the Fock basis, which explicitly shows the ’raising’ and ’lowering’ properties of these operators with respect to photon number states. To the best of our knowledge, this is the first experimental demonstration of complete tomography of trace-non-preserving quantum processes.

All output states are characterized through their corresponding Wigner functions. Results are also validated through theoretical modeling. Furthermore, the photon addition and subtraction operations are characterized through the diagonal elements of the process tensors and are validated through theoretical generated data using Monte Carlo simulation.

Acknowledgments

It goes without saying that I had a wonderful time during my master's program and I would like to thank entire IQIS and PHAS for making this happen.

I would like to thank my supervisor Alex Lvovsky for sharing his knowledge and expertise in the field of quantum optics. I would also like to thank my colleagues for their help in the lab and through stimulating discussions; without their help it would have been a much challenging task to work in the lab. It includes Nitin Jain, Attie Hendriks, Andrew MacRae, Connor Kupchak, Pantita Palittapongarnpim, Ryan Thomas, Travis Brannan and Jose Hipolito Garcia Gracia.

A special thanks goes to Erick Barrios for helping me out in the experiment and Aamir Anis for developing the algorithm for Quantum process tomography using Maximum-likelihood estimation - it made my data processing task relatively much simpler.

In the end, I would like to express my gratitude to my family and friends for their patience and support during my studies.

Table of Contents

List of Tables

List of Figures

Chapter 1

Overview

Quantum operators of annihilation $\hat{a}$ and creation $\hat{a}^\dagger$ of bosonic particles act on states with a definite number m of identical particles, resulting in that number being incremented or decremented, respectively:

$$\begin{aligned} \hat{a}^\dagger \mid m\rangle &= \sqrt{m+1} \mid m+1\rangle \\ \hat{a} \mid m\rangle &= \sqrt{m} \mid m-1\rangle \end{aligned} \tag{1.1}$$

First proposed by Dirac in his 1927 Quantum Theory of the Emission and Absorption of Radiation [1], these operators play an enormous role in many fields of physics and chemistry: quantum mechanics, quantum optics, quantum chemistry, quantum field theory and condensed matter physics. Specializing to optics, they are instrumental in quantum description of light, giving rise to theory of fundamental phenomena such as spontaneous emission and lasing. Equally important is practical implementation of photon creation and annihilation, which provides us with a universal toolbox for manufacturing arbitrary quantum states of light, required for quantum information processing and quantum communications [2, 3].

Implementation of these operators is however challenging. This is because $\hat{a}$ and $\hat{a}^\dagger$ do not preserve the trace of a state's density matrix, which means they cannot occur in the framework of deterministic Hamiltonian evolution of a physical system. Therefore realization of bosonic creation and annihilation is only possible in an approximate, non-deterministic fashion. That is, the action of operators occurs with probability less than one, but is heralded by a classical event. This method has been employed in the context of traveling optical photons. First successful realization of the photon creation operator by Zavatta et al. [2] gave rise to a new class of states known as photon added states.

In 2006, Ourjoumtsev and colleagues applied the photon annihilation operation to the squeezed states generating optical ”Schrødinger cats” [3]. Neergaard-Nielsen et al. generalized this approach in 2010 to generating arbitrary continuous-variable qubits [4]. In 2007, Parigi et al. verified non-commutativity of $\hat{a}$ and $\hat{a}^\dagger$ in application to the thermal state [5].

In order to include the photon creation and annihilation operations into the quantum technology toolbox, we need to develop methods of their characterization and performance testing. This is the purpose of the present work. We implement $\hat{a}$ and $\hat{a}^\dagger$ experimentally and analyze them as quantum ”black boxes”, or quantum processes. By probing them with coherent optical states (weak laser pulses) of different amplitudes and measuring the quantum fluctuations of the output electromagnetic field, we determine how these black boxes would affect any arbitrary state of light within a practically relevant subspace of the optical Hilbert space [6]. In particular, for the first time since the photon creation and annihilation operators have been discovered, we explicitly observe their action on the photon number states to be in accordance with Eq. 1.1.

The method employed for the characterization of quantum processes relies on the optical equivalence theorem [6]. According to that theorem, the density operator of an arbitrary state can be written as a linear combination of coherent-state density operators,

$$\hat{\rho} = \int P_{\hat{\rho}}(\alpha) \mid \alpha\rangle\langle\alpha \mid d^2\alpha, \tag{1.2}$$

where $P_{\hat{\rho}}(\alpha)$ is the Glauber-Sudarshan P function of state $\hat{\rho}$ [7]. Further, since every quantum process $\mathcal{E}$ (in this case, photon creation and annihilation) is a linear map with respect to density matrices, we can write the process output as

$$\mathcal{E}(\hat{\rho}) = \int P_{\hat{\rho}}\mathcal{E}(\mid \alpha\rangle\langle\alpha \mid)d^2\alpha. \tag{1.3}$$

This is useful because optical states that are employed in quantum information processing (for example, number states or their superpositions) are highly non-classical and cannot be generated easily. In contrast, coherent states are directly obtained from lasers. Our method permits us, by probing the ”black box” with simple laser pulses, to learn about its response to any other state of light, however complicated it may be.

This method is referred to as coherent-state quantum process tomography (csQPT) [6, 8, 9]. The result of csQPT — the data about the process — can be compactly written in the form of a rank-4 ”process tensor” $\mathcal{E}_{jk}^{mn}$, defined according to $[\rho_{\text{out}}]_{jk} = \sum_{m,n} \mathcal{E}_{jk}^{mn} [\rho_{\text{in}}]_{mn}$, where ρ_{in} and ρ_{out} denote, respectively, the density matrices of the input and output states in the photon number basis. The process tensor is calculated according to

$$\mathcal{E}_{jk}^{mn} = \int P_{mn}(\alpha)\langle j \mid \mathcal{E}(\mid \alpha\rangle\langle\alpha \mid) \mid k\rangle d^2\alpha, \tag{1.4}$$

where $P_{mn}(\alpha)$ is the P function of operator $|m\rangle\langle n|$. Computation of the process tensor is complicated by highly singular nature of this function; Refs [6, 8, 9] elaborate different ways of resolving this singularity. Another practical issue is associated with the infinite dimension of the optical Hilbert space. In csQPT experiments, the process tensor is evaluated for a subspace $\mathcal{H}(n_{\text{max}})$ spanned by number states up to a certain cut-off value, n_{max}. The choice of n_{max} is determined by the maximum amplitude α_{max} of the set of coherent probe states used in the experiment, as well as the reconstruction method used. In our experiment, $n_{\text{max}} = 5$.

This thesis is organized as follows: Chapter 2 provides an introduction to quantum states of light field and presents basic concepts like the Wigner function and the method of optical homodyne tomography. Further, it gives an introduction to quantum state tomography (QST) followed with the description of non-linear process such as parametric down conversion; and the implementation of photon creation ($\hat{a}^\dagger$) and annihilation ($\hat{a}$) operators. In the end, it provides a brief introduction and in-depth implementation of Quantum process tomography (QPT) using *maximum likelihood estimation*.

Chapter 3 starts with the experimental realization of single photon source, which is crucial for the realization of photon creation operation. This chapter covers the experimental realization of quantum process tomography for photon creation and annihilation operators. Results and practical challenges of experimental QPT are presented in detail.

Chapter 4 is the final chapter of this thesis, which covers the summary and outlook of the present work.

Chapter 2

Theoretical Concepts

2.1 Quantum Theory of Light

Light has proven to be an excellent media to prove the fundamentals of quantum mechanics, it shows both wave and particle aspects [7]. Light has been observed to show the characteristics of wave through interference and dispersion, as well as characteristics of particle through distinct detector clicks when detected with high precision detector. This thesis is concerned with the quantum nature of the light and since classical theories cannot describe the quantum aspect of the light field - we will make extensive use of a quantum mechanical treatment.

2.1.1 Quantization of light field

Suppose $\vec{A}(\vec{r},t)$ is the electromagnetic vector potential of the electromagnetic field and $\phi(\vec{r},t)$ is the electromagnetic scalar potential in a large evacuated box with volume $V = L_x \times L_y \times L_z$[10]:

$$\begin{aligned}\vec{A}(\vec{r},t) &= \sum_s \int d^3k a_{\vec{k},s} \vec{s}\, u(\vec{r}) e^{i(\vec{k}.\vec{r}-\omega t)} + h.c., \qquad (2.1)\\ \vec{E}(\vec{r},t) &= -\nabla\phi(\vec{r},t) - \frac{\partial}{\partial t}\vec{A}(\vec{r},t),\\ \vec{B}(\vec{r},t) &= \nabla \times \vec{A}(\vec{r},t),\end{aligned}$$

where $a_{\vec{k},s}$ is the field amplitude, $\vec{s}$ the polarization vector, $\vec{k}$ is the unit k-vector and $u(\vec{r})$ the normalized transverse Gaussian mode of the light field. $\sum_s$ denotes the summation of the two orthogonal polarizations. After solving Eq. 2.1, we have,

$$\begin{aligned}\vec{E}(\vec{r},t) &= \sum_{\vec{k},s} e^{i\vec{k}\vec{r}} \vec{u}_{\vec{k},s}(t) + c.c; \qquad (2.2)\\ \vec{B}(\vec{r},t) &= \sum_{\vec{k},s} e^{i\vec{k}\vec{r}} \vec{\omega}_{\vec{k},s}(t) + c.c,\end{aligned}$$

where $\vec{u}_{\vec{k},s}(t)$ and $\vec{\omega}_{\vec{k},s}(t)$ are the time-dependent amplitudes of the electric and magnetic fields.

Any arbitrary electromagnetic field configuration inside the box can be decomposed in the form of Eq. (2.2) and because the box is of a finite size, it is sufficient to use a series over a discrete set of wave-vectors $\vec{k} = (2\pi n_x/L_x, 2\pi n_y/L_y, 2\pi n_z/L_z)$ (where n_x, n_y, n_z) are arbitrary natural numbers), rather than an integral. The behavior of the field in space is given by a periodic function whose periods in the three dimensions are equal to L_x, L_y and L_z.

In order to quantize the mode, we begin by writing its energy (Hamiltonian) H in terms of the field amplitudes. We then define the *position* x and *momentum* p that satisfy the classical *canonical equations of motion*

$$\begin{aligned} \dot{p} &= -\frac{\partial H}{\partial x}; \\ \dot{x} &= \frac{\partial H}{\partial p}. \end{aligned} \tag{2.3}$$

In transition from classical to quantum mechanics, the canonical position and momentum give rise to operators whose commutator is equal to

$$[\hat{x}, \hat{p}] = i\hbar. \tag{2.4}$$

In quantum optics, the convention is slightly different. We define the position and momentum according to $X = x/\sqrt{\hbar}, P = p/\sqrt{\hbar}$. Then the canonical equations of motion takes the form

$$\begin{aligned} \dot{P} &= -\frac{\partial H}{\partial X}; \\ \dot{X} &= \frac{\partial H}{\partial P} \end{aligned} \tag{2.5}$$

and the commutator

$$[\hat{X}, \hat{P}] = i. \tag{2.6}$$

The classical Hamiltonian of the electromagnetic field

$$H = \int d^3r\, (\epsilon_0 \vec{E}^2 + \frac{1}{\mu_0}\vec{B}^2), \tag{2.7}$$

can be rewritten in terms of *canonical variables*

$$\begin{aligned} X_{\vec{k},s} &= \sqrt{\epsilon_0 V(\hbar\omega_{\vec{k}})^{-1}}(u_{\vec{k},s}(t) + u_{\vec{k},s}(t)^*); \\ P_{\vec{k},s} &= \sqrt{\epsilon_0 V(i^2\hbar\omega_{\vec{k}})^{-1}}(u_{\vec{k},s}(t) - u_{\vec{k},s}(t)^*), \end{aligned} \tag{2.8}$$

where $\omega_{\vec{k}} = ck$ and the $\vec{u}$'s are treated as scalars then the Hamiltonian takes the form

$$H = \sum_s d^3k \, \frac{\hbar\omega}{2}(X^2_{\vec{k},s} + P^2_{\vec{k},s}). \tag{2.9}$$

From here onward, we will be concerned only with one specific mode and hence, indices $(\vec{k}, s)$ can be omitted. The position and momentum operators have eigenstates, $|X\rangle$ and $|P\rangle$, respectively, which are related to[1]

$$\begin{aligned} \langle X|X^{'}\rangle &= \delta(X - X^{'}); \\ \langle P|P^{'}\rangle &= \delta(P - P^{'}). \end{aligned} \tag{2.10}$$

The position and momentum eigenstates are related to each other via the *de Broglie wave*:

$$\langle X|P\rangle = \frac{1}{\sqrt{2\pi}} e^{iPX}, \tag{2.11}$$

so for an any arbitrary state $|\psi\rangle$

$$\begin{aligned} \langle X|\psi\rangle &= \frac{1}{\sqrt{2\pi}} \int_{-\infty}^{+\infty} \langle P|\psi\rangle e^{iPX} dP; \\ \langle P|\psi\rangle &= \frac{1}{\sqrt{2\pi}} \int_{-\infty}^{+\infty} \langle X|\psi\rangle e^{iPX} dX. \end{aligned} \tag{2.12}$$

In other words, the wave functions of a given state $|\psi\rangle$ in the position and momentum representations are direct and inverse Fourier transforms of each other. In optics $\hat{X}$ and $\hat{P}$ correspond to the *in-phase* and *out-of-phase* component of the electric field amplitude of the spatial-temporal mode (with respect to a reference phase).

---

[1] Because these states are not normalizable, they, strictly speaking, belong not to the Hilbert space, but to the so-called *rigged Hilbert space*. See R. de la Madrid, Eur. J. Phys. 26, 287-312 (2005) for details.

2.1.2 Photon creation and annihilation operator

At this point, we can define canonical variables $\hat{X}$ and $\hat{P}$ in terms of non-hermitian photon creation ($\hat{a}^{\dagger}$) and annihilation ($\hat{a}$) operators, such that

$$\begin{aligned} \hat{X} &= \frac{(\hat{a}^{\dagger} + \hat{a})}{\sqrt{2}}; \\ \hat{P} &= \frac{i(\hat{a}^{\dagger} - \hat{a})}{\sqrt{2}} \end{aligned} \tag{2.13}$$

and using Eq. (2.13) in Eq. (2.6), we have

$$[\hat{a}, \hat{a}^{\dagger}] = 1. \tag{2.14}$$

Using the *photon-number* operator $\hat{n} \equiv \hat{a}^{\dagger}\hat{a}$ that accounts for the photons in the chosen single mode of a light field, the Hamiltonian in Eq. (2.9) can be rewritten as

$$\hat{H} = (\hat{n} + \frac{1}{2}). \tag{2.15}$$

2.1.3 Fock states

Let us now introduce Fock states $|n\rangle$ as the eigen states of photo-number operator

$$\hat{n}|n\rangle = n|n\rangle. \tag{2.16}$$

We can show if $|n\rangle$ is an eigen state of $\hat{n}$, then $\hat{a}|n\rangle$ and $\hat{a}^{\dagger}|n\rangle$ must also be the eigenstates of $\hat{n}$ with eigenvalue (n - 1) and (n + 1), respectively.

$$\begin{aligned} \hat{n}\hat{a}|n\rangle &= \hat{a}^{\dagger}\hat{a}^{2}|n\rangle = (\hat{a}\hat{a}^{\dagger}\hat{-}\hat{a})|n\rangle = (n-1)\hat{a}|n\rangle; \\ \hat{n}\hat{a}^{\dagger}|n\rangle &= \hat{a}^{\dagger}\hat{a}\hat{a}^{\dagger}|n\rangle = (\hat{a}^{\dagger} + \hat{a}^{\dagger}\hat{a}^{\dagger}\hat{a})|n\rangle = (n+1)\hat{a}^{\dagger}|n\rangle. \end{aligned} \tag{2.17}$$

Eq. (2.17) give rise to two fundamental relations

$$\begin{aligned} \hat{a}|n\rangle &= \sqrt{n}|n-1\rangle; \\ \hat{a}^{\dagger}|n\rangle &= \sqrt{n+1}|n+1\rangle. \end{aligned} \tag{2.18}$$

2.1.4 Coherent state

Coherent state is very crucial for this thesis because it has been used as a probe state for quantum process tomography (see section 2.6) [6, 8, 9]. It is also an important state of the harmonic oscillator, whose behavior is very similar to that of a classical oscillating particle with well behaved amplitude $|\alpha|$ and phase $\arg \alpha$.

Coherent state is defined as the eigenstates of the annihilation operator $\hat{a}$

$$\hat{a}|\alpha\rangle = \alpha|\alpha\rangle, \tag{2.19}$$

where α is a complex number.[2]

Displacement operator

Even for $\alpha = 0$, Eq. (2.19) is valid, implying vacuum is a coherent state as well. In other words, vacuum is a zero-amplitude coherent state.We can calculate from Eq. (2.15) that the mean energy of a coherent state is simply

$$\langle\hat{H}\rangle = \langle\alpha|\hat{a}^\dagger\hat{a} + \frac{1}{2}|\alpha\rangle = |\alpha|^2 + \frac{1}{2}. \tag{2.20}$$

Now, we introduce *displacement operator*, which will help us to understand the relation between coherent state and vacuum. We define displacement operator as

$$\hat{D}(\alpha) = \exp(\alpha\hat{a}^\dagger - \alpha^*\hat{a}) \tag{2.21}$$

and because $i(\alpha\hat{a}^\dagger - \alpha^*\hat{a})$ is Hermitian, $\hat{D}$ must be unitary. The displacement operator displaces the amplitude $\hat{a}$ by the complex amplitude α as

$$\hat{D}^\dagger(\alpha)\hat{a}\hat{D}(\alpha) = \hat{a} + \alpha \tag{2.22}$$

and for negative displacement to $|\alpha\rangle$ in Eq. (2.19), we have

$$\hat{a}\hat{D}(-\alpha)|\alpha\rangle = \hat{D}(-\alpha)\hat{D}^\dagger(-\alpha)\hat{a}\hat{D}(-\alpha)|\alpha\rangle = \hat{D}(-\alpha)(\hat{a} - \alpha)|\alpha\rangle, \tag{2.23}$$

---

[2] Complex eigenvalues are allowed because $\hat{a}$ is non-Hermitian.

which must be equal to zero from Eq. (2.19), which implies $\hat{D}(-\alpha)|\alpha\rangle$ is the vacuum state $|0\rangle$. So, in other words coherent states are *displaced vacuums*

$$|\alpha\rangle = \hat{D}(\alpha)|0\rangle. \tag{2.24}$$

Some other properties of coherent states

Any coherent state $|\alpha\rangle$, is a state of the harmonic oscillator and can therefore be decomposed in the basis of $|n\rangle$, which means

$$|\alpha\rangle = \sum_{n=0}^{\infty}\langle n|\alpha\rangle|n\rangle \tag{2.25}$$

and we can also write

$$\langle n|\alpha|\alpha\rangle = \alpha\langle n|\alpha\rangle. \tag{2.26}$$

On the other hand using Eq. (2.19), we have

$$\langle n|\alpha|\alpha\rangle = \langle\alpha|a^{\dagger}|n\rangle^{*} = \sqrt{n+1}\langle\alpha|n+1\rangle^{*}. \tag{2.27}$$

Now after equating Eq. (2.26) and Eq. (2.27), we have

$$\langle n+1|\alpha\rangle = \frac{\alpha}{\sqrt{n+1}}\langle n|\alpha\rangle. \tag{2.28}$$

Starting from the lowest $n = 0$, by induction we have

$$\langle n|\alpha\rangle = \frac{\alpha^{n}}{\sqrt{n!}}\langle 0|\alpha\rangle, \tag{2.29}$$

which enables us to represent $|\alpha\rangle$ as

$$|\alpha\rangle = \langle 0|\alpha\rangle\sum_{n=0}^{\infty}\frac{\alpha^{n}}{\sqrt{n!}}|n\rangle, \tag{2.30}$$

where the only unknown is a constant factor $\langle 0|\alpha\rangle$, a complex number. In order for $|\alpha\rangle$ to be normalized, $\langle\alpha|\alpha\rangle = 1$, we have

$$\langle\alpha|\alpha\rangle = |\langle 0|\alpha\rangle|^{2}\sum_{n=0}^{\infty}\frac{|\alpha|^{2n}}{n!} = |\langle 0|\alpha\rangle|^{2}\exp(|\alpha|^{2}) = 1. \tag{2.31}$$

From Eq. (2.30) and Eq. (2.31) we have

$$|\alpha\rangle = e^{-\frac{1}{2}|\alpha|^2} \sum_{n=0}^{\infty} \frac{\alpha^n}{\sqrt{n!}} |n\rangle. \tag{2.32}$$

Eq. (2.32) is a very important result because using this equation we can express coherent state with arbitrary amplitude $|\alpha\rangle$ in Fock-basis.

Before we proceed further, let us find the physical meaning of the complex parameter α. From Eq. (2.19) it is apparent that $|\alpha|$ is related to the amplitude of the field. The expectation value of the photon number $\hat{n} = \hat{a}^{\dagger}\hat{a}$

$$\bar{n} = \langle\alpha|\hat{n}|\alpha\rangle = |\alpha|^2 \tag{2.33}$$

and thus $|\alpha|^2$ is just the average number of the photons in the field. To find the fluctuations of the photon number we need to calculate

$$\begin{aligned} \langle\alpha|\hat{n}^2|\alpha\rangle &= \langle\alpha|\hat{a}^{\dagger}\hat{a}\hat{a}^{\dagger}\hat{a}|\alpha\rangle, \\ &= \langle\alpha|\hat{a}^{\dagger}\hat{a}^{\dagger}\hat{a}\hat{a} + \hat{a}^{\dagger}\hat{a}\alpha\rangle, \\ &= |\alpha|^4 + |\alpha|^2 \end{aligned} \tag{2.34}$$

and thus

$$\Delta n = \sqrt{\langle\hat{n}^2\rangle - \langle\hat{n}\rangle^2} = \bar{n}^{\frac{1}{2}}, \tag{2.35}$$

which is characteristics of a Poissonian statistics.

Also from (2.32), the probability of detecting n photons is

$$P_n = |\langle n|\alpha\rangle|^2 = e^{-|\alpha|^2}\frac{|\alpha|^{2n}}{n!} \quad = e^{-\bar{n}}\frac{\bar{n}^n}{n!}, \tag{2.36}$$

which is a Poisson distribution with a mean $\bar{n}$. Note that the fractional uncertainty in the photon number is

$$\frac{\Delta n}{\bar{n}} = \frac{1}{\sqrt{\bar{n}}}. \tag{2.37}$$

Counting the photons of a coherent state means making repeated measurements on a statistical ensemble of identically prepared fields. Each time, n photons are obtained with Poissonian probability P_n, and on average we get as many photons as quantified by the intensity $|\alpha|^2$. This behavior is similar to classical particles when they are taken at random from a pool with an average of $|\alpha|^2$ each time. We may say that when the photons of a coherent state are counted they behave like randomly distributed classical particles.

We should also note that coherent states are not exactly orthogonal. In fact, we obtain from Fock representation Eq. (2.32)

$$\begin{aligned} \langle\alpha^{'}|\alpha\rangle &= \exp(-\frac{|\alpha|^2}{2} - \frac{|\alpha^{'}|^2}{2})\sum_{n=0}^{\infty}\frac{(\alpha^{'*}\alpha)^n}{n!} && (2.38) \\ &= \exp(-\frac{|\alpha|^2}{2} - \frac{|\alpha^{'}|^2}{2} + \alpha^{'*}\alpha) && (2.39) \end{aligned}$$

and consequently

$$|\langle\alpha^{'}|\alpha\rangle|^2 = \exp(-|\alpha - \alpha^{'}|^2) \tag{2.40}$$

The Gaussian in Eq. (2.40) goes rapidly to zero when the amplitudes α and $\alpha^{'}$ differ significantly more than the quadrature-noise level of the vacuum. We also note that coherent states are over complete,

$$\int_{-\infty}^{+\infty}\int_{-\infty}^{+\infty}|\alpha\rangle\langle\alpha|\frac{dq_0dp_0}{2\pi} = 1. \tag{2.41}$$

This is, we may express any state in the coherent-state basis. (Coherent states are even overcomplete because fewer than all of them form a basis already. This property is a side effect of their lack of strict orthogonality.

Optical equivalence theorem

Optical equivalence theorem is a method to writing down a density matrix ($\hat{\rho}$) of any arbitrary state as a linear combination of coherent-state density operators.

$$\hat{\rho} = \int P_{\hat{\rho}}(\alpha) \mid \alpha\rangle\langle\alpha \mid d^2\alpha, \tag{2.42}$$

where $P_{\hat{\rho}}(\alpha)$ is the Glauber-Sudarshan P function of state $\hat{\rho}$ [7]. Eq. 2.42 might seem puzzling because this expression implies any pure state $|\psi\rangle$ can be written as a statistical mixture of coherent state even though the state in question is non-classical. The answer to this paradox is " ill-behaved" P-function for non-classical states. We will see in later section, even though our method for quantum process tomography relies on optical equivalence theorem, we do not involve P-function in our experimental calculations and that makes our method versatile.

2.1.5 Wigner function

In classical optics the state of an electromagnetic oscillator is perfectly described by the statistics of the classical amplitude α. The amplitude may be completely fixed (the field is coherent), or α may fluctuate (then the field is partially coherent or incoherent). In classical optics as well as in classical mechanics, we can characterize the statistics of the complex amplitude α or, equivalently, the statistics of the component position X and momentum P by introducing a phase-space distribution $W(X, P)$. The distribution $W(X, P)$ quantifies the probability of finding a particular pair of X and P values in their simultaneous measurement. Knowing the phase-space probability distribution, all statistical quantities of the electromagnetic oscillator can be predicted by calculation. In this sense, the phase-space distribution describes the state in classical physics.

Quantum system cannot be described by a point in phase-space; however, there exist a phase-space distribution very much like a probability density distribution for a classical system. A very powerful and widely used phase-space representation is the Wigner function, which was first introduced by E. Wigner in a famous paper dating back to 1932 [11].

Suppose now, that every time the particle is prepared, we measure the observable

$$X_\theta = X\cos\theta + P\sin\theta. \tag{2.43}$$

Based on the data obtained in this measurement, we can construct a *histogram* of the experimental results, also known as *marginal distribution* $\mathrm{pr}(X_\theta)$. This marginal distribution is

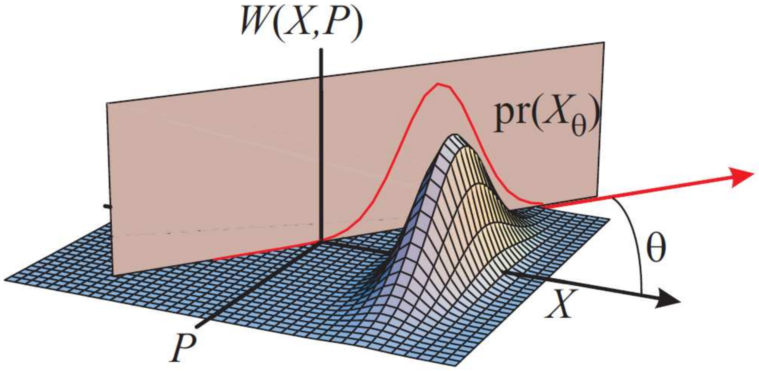

Figure 2.1: Phase-space probability density and marginal distribution.

the integral projection of the phase-space probability density on the vertical plane oriented at angle θ with respect to the vertical axis (Fig. 2.1)

$$\mathrm{pr}(X_\theta) = \int_{-\infty}^{+\infty} W(X\cos\theta - P\sin\theta, X\sin\theta + P\cos\theta)dP. \tag{2.44}$$

In the quantum domain for any state there is an analog called phase space quasi-probability distribution function (or Wigner function), it is similar to a classical probability distribution function of values of X and P, but it can become negative. In any case, the marginal distribution associated with a particular quantum state and a particular quadrature is a projection of the state's Wigner function upon a vertical plane (Fig. 2.1).

The marginal distributions $\int_{-\infty}^{+\infty} W(X,P)\mathrm{d}P$ or $\int_{-\infty}^{+\infty} W(X,P)\mathrm{d}X$ give us the position or momentum distributions respectively. If we perform multiple quantum measurements of a *single* quadrature on a set of identical quantum states we will obtain the marginal distribution associated with the quadrature, and additionally, if we perform a phase shift θ, the components X and P rotate in the two dimensional phase space (X, P). So, we can find that $\mathrm{pr}(X,\theta)$ after an arbitrary phase shift θ [7]:

$$\mathrm{pr}(X,\theta) = \langle X|\hat{U}(\theta)\hat{\rho}\hat{U}^\dagger(\theta)|X\rangle = \int_{-\infty}^{+\infty} W(X\cos\theta - P\sin\theta, X\sin\theta + P\cos\theta)dP, \tag{2.45}$$

where $\hat{U}(\theta) \equiv \exp(-i\theta\hat{n})$ is the phase shifting operator. Eq. (2.45) is the connection of $W(X,P)$

to observables quantities and it links quantum states (its density matrices, $\hat{\rho}$) with observables. Considering the special cases $\theta = 0$ and $\theta = \frac{\pi}{2}$ we see that the marginal distributions of $W(X, P)$ produce the correct position and momentum probabilities respectively

$$\begin{aligned} \theta &= 0 \Rightarrow \int_{-\infty}^{+\infty} W(X,P)\mathrm{d}P = \langle X|\hat{\rho}|X\rangle; \\ \theta &= \frac{\pi}{2} \Rightarrow \int_{-\infty}^{+\infty} W(X,P)\mathrm{d}P = \langle P|\hat{\rho}|P\rangle. \end{aligned} \tag{2.46}$$

Integrals such as in Eq. (2.45) are called *Radon transformations*. Inverse Radon transformations turns out to be the mathematical key for quantum state reconstruction. $W(X, P)$ is closely related to the density matrix ($\hat{\rho}$) through the famous classical-like phase-space distribution (2.47) in quantum mechanics called the Wigner function [11, 7].

$$W_{\hat{\rho}}(X,P) = \frac{1}{(2\pi)} \int_{-\infty}^{+\infty} \exp(iqP)\langle X - \frac{q}{2}|\hat{\rho}|X + \frac{q}{2}\rangle dq. \tag{2.47}$$

It is a real function if $\hat{\rho}$ is Hermitian, and it is normalized

$$\int\int_{-\infty}^{+\infty} W_{\hat{\rho}}(X,P)dXdP = 1. \tag{2.48}$$

E. Wigner chose this function from the set of possible quasi-probability distribution, since from all possible phase space distribution it seemed to be the simplest. Its popularity most likely derives from the fact that its marginal distribution, obtained by integrating along a particular direction in phase space yields the measurable quadrature of the field.

The Wigner function has proven to be a very helpful visualization of a quantum mechanical system in phase space. It is normalized and its marginal distributions $\mathrm{pr}(X_\theta)$ – the density shadows of the Wigner function are equal to the quadrature amplitude probability density of the system.

We see that the quantum phase-space quasi-probability density inherits most of its properties from its classical counterpart. One difference of the quantum case is that the Wigner function is allowed to take on negative values (e.g. with the single photon Fock state). This is because the Wigner function no longer has the meaning of a probability distribution. The marginals of the Wigner function, however, do have a meaning of measurable probability densities even in the quantum case. So whenever the Wigner function has a negative well, it must be surrounded by a positive hill so all its projections are non-negative.

One can define the Wigner function for any operator, rather than just density operators, by analogy with 2.47. However, the Wigner function of an arbitrary operator is not necessarily real and normalized.

Examples of Wigner function:

Using 2.47 we can find the Wigner function for any arbitrary state.

1. Vacuum state

$$W_0(X,P) = \pi^{-1}\exp(-X^2 - P^2). \tag{2.49}$$

$W(X,P)$ turned out to be Gaussian (see figure 2.2).

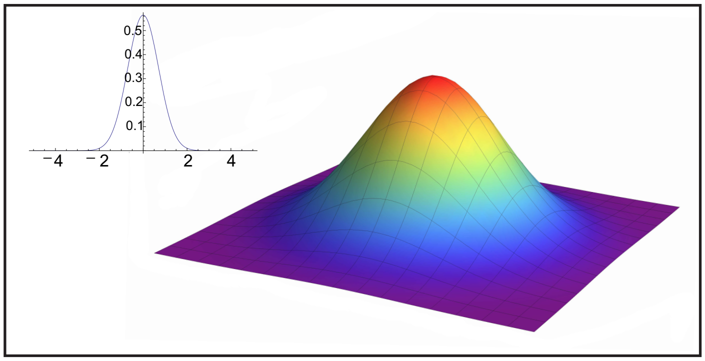

Figure 2.2: Wigner function of vacuum, *Inset*: Marginal distribution for $\theta = 0$

1. Single photon Fock state

$$W_1(X,P) = \pi^{-1}\exp(-X^2 - P^2)(2X^2 + 2P^2 + 1). \tag{2.50}$$

$W(X,P)$ turns out to be negative, which is a signature of non-classical state (see figure 2.3).

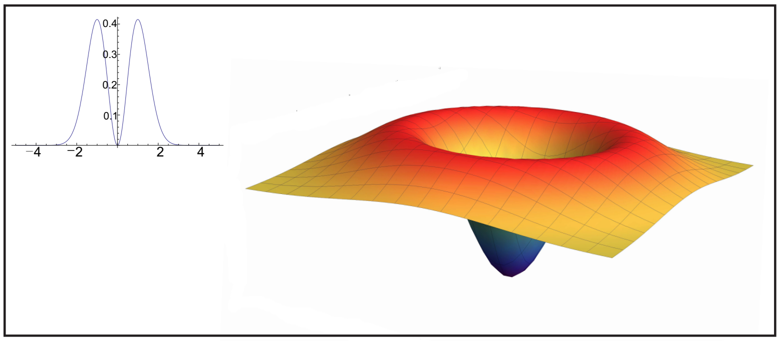

Figure 2.3: Wigner function of single photon fock state, *Inset*: Marginal distribution for $\theta = 0$

2.2 Non-linear Process

2.2.1 Parametric down conversion

Spontaneous parametric down-conversion (SPDC): A nonlinear crystal ”splits” an incoming photons into two a pair of photons of lower energy, whose combined energy and momentum is equal to the energy and momentum of the original photon. The process is spontaneous in the same sense as spontaneous emission, it is stimulated by random vacuum fluctuations. Consequently, the photon pairs are created at random times. However, if one of the pair (the ”signal”) is detected at any time then we know its partner (the ”idler”) is present as well. This is an excellent source of single photon, first demonstrated by Hong *et. el* in 1986 [14].

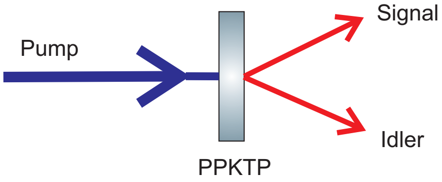

Figure 2.4: Parametric down conversion using non-linear crystal.

Spontaneous parametric down-conversion can be viewed as a coherent three-photon process, where a crystal which is not centro-symmetric is illuminated by a pump beam. The pump beam is intense enough to drive the oscillations of the electrons in the crystal into the nonlinear regime. The second order interaction results in the annihilation of a pump photon and the creation of the two down-converted photons termed the signal and idler. The photons pair that are created are entangled in space-time or, equivalently, in wave number and frequency. The energy and momentum conservation can be described by the equations:

$$\begin{aligned} \hbar\omega_p &= \hbar\omega_s + \hbar\omega_i; \\ \hbar\vec{k}_p &= \hbar\vec{k}_s + \hbar\vec{k}_i, \end{aligned} \tag{2.51}$$

where frequency and wave-number are related by $|\vec{k}(\omega)| = n(\omega)\omega/c; n(\omega)$ being the frequency-dependent refractive index.

The photon pairs created in SPDC are highly entangled in wave number and frequency [15, 16]. Furthermore, if they possess the same polarization, then the process is termed type I spontaneous parametric down conversion. Conversely, the case of orthogonal polarization of signal and idler photons - generally corresponding to the signal (idler) electric field being ordinary (extraordinary) waves in a birefringent crystal is a type II process.

Interaction Hamiltonian and time evolution

The parametric down-conversion interaction Hamiltonian can be expressed as [18]

$$\hat{H}_{\mathrm{PDC}} = i\lambda\hbar(\hat{a}_s^\dagger\hat{a}_t^\dagger - \hat{a}_s\hat{a}_t), \tag{2.52}$$

where λ is proportional to the amplitude of the (classical) pump and to the second-order susceptibility of the medium. $\zeta = \lambda\tau/\hbar$ has the meaning of squeezing parameter and τ being the fictitious interaction time. If $|\zeta| \ll 1$, which is the case on our experiment, the evolution of Hamiltonian (2.52) can be approximated as

$$e^{-i\hat{H}\tau/\hbar} \approx 1 - i\hat{H}\tau/\hbar. \tag{2.53}$$

For now, if we assume the initial state in the signal and idler modes to be vacuum, i.e. $|\psi_0\rangle = |0_s\rangle \otimes |0\rangle_i$. The evolution operator, acting on this state, yields

$$e^{-i\hat{H}_{\mathrm{PDC}}\tau/\hbar}\,|0\rangle_s\,|0\rangle_t \approx |0\rangle_s\,|0\rangle_t + \zeta\,|1\rangle_s\,|1\rangle_t\,, \tag{2.54}$$

which projects onto the signal state $|1\rangle_s$, if a trigger photon is detected.

The above treatment is valid as long as higher-order terms in the Taylor decomposition (2.53) can be neglected. This is the case when $|\zeta| \ll 1$. If they are also degenerate in their respective center frequencies[3], the output state (ignoring the vacuum term in the sum) is essentially an outer product of two single-photon Fock states, entangled in frequency and wavenumber (but not in polarization, because of collinearity [16]).

2.3 Implementation of Photon Creation and Annihilation Operators

In the earlier section, we observed the classical nature of coherent state $|\alpha\rangle$ as well as the quantum-mechanical nature of Focks states $|n\rangle$. Now, in this section we will look into the properties of state intermediate between the Fock state and the coherent state. Such state can be obtained by application of photon creation operator ($\hat{a}^\dagger$) on coherent state and has shown to exhibit non-classical properties like sub-Poissonian photon statistics [19]. On the other hand, implementation of photon annihilation operator ($\hat{a}$) on coherent is a direct verification of its definition as eigenstates of $\hat{a}$ (2.19) and this implies, the final state still exhibits classical features.

Photon creation and annihilation operator can also be viewed as a universal toolbox for manufacturing arbitrary quantum states of light, required for quantum information processing and quantum communication.

---

[3] i.e. $\omega_{cs} = \omega_{ci} = 0.5\omega_{cp}$, the additional subscript c denotes the central frequency

2.3.1 Photon creation operator

Generation of the photon added states

Photon added states can be generated by injecting a target state $|\psi\rangle$ into the signal mode of an optical parametric amplifier and exploiting the stimulated emission of a single down-converted photon into the same mode. Hence, we can herald the generation of the target state in the signal channel by detecting single photon in the correlated idler channel [20].

The Hamiltonian for the parametric amplifier reads as

$$\hat{H} = i\hbar\lambda(\hat{a}_s^\dagger \hat{a}_i^\dagger - \hat{a}_s\hat{a}_i), \tag{2.55}$$

where $\hat{a}_i$ ($\hat{a}_s$) is the annihilation operator for the idler (signal) mode and λ is proportional to the amplitude of the (classical) pump and to the second-order susceptibility of the medium.If the parametric gain is kept sufficiently low ($\zeta = \lambda\tau/\hbar \ll 1$, τ being the fictitious interaction time) and letting a seed target field $|\psi\rangle_s$ enter the parametric crystal in the signal mode, while vacuum ($|0\rangle_i$) enters in the idler channel, which is the case for our experimental situation, the final output state can be approximated as

$$|\psi\rangle = [1 + \zeta(\hat{a}_s^\dagger \hat{a}_i^\dagger - \hat{a}_s\hat{a}_i)]|\psi\rangle_s|0\rangle_i = |\psi\rangle_s|0\rangle_i + \zeta\hat{a}_s^\dagger|\psi\rangle_s|1\rangle_i \tag{2.56}$$

which projects onto the signal state $\hat{a}_s^\dagger\,|\psi\rangle_s$ if a trigger photon is detected. The above treatment is valid as long as $\zeta n_{|\psi\rangle} \ll 1$, with $n_{|\psi\rangle}$ being the mean photon number in the target state.

If the input target state is coherent state $|\alpha\rangle$ in the signal mode then the output signal mode will mostly contain the original target coherent state, except for the few cases when the state $|1\rangle_i$ is detected in the idler output mode with a probability proportional to $|\zeta|^2(1 + |\alpha|^2)$, projects the signal state onto the single photon added coherent state (SPACS) $|\alpha, 1\rangle_s$, corresponding to the stimulated emission of one photon in the same mode of $|\alpha\rangle$. This implies $\mathrm{Pr}_{\hat{a}^\dagger} = 1 + \alpha^2$.

It is important to note that, when there is no input coherent state in the non-linear crystal then after SPDC, we will only have the pair of entangled photons $|1\rangle_s|1\rangle_i$ with a low probability proportional to $|\zeta|^2$. In this case, the detection of a single photon in the idler channel projects the signal state onto a single-photon Fock state and, by following the evolution of the final quantum state while the amplitude α increases from zero, one can witness the gradual transition from the spontaneous to the stimulated regimes of light emission with the smooth transformation of a single photon (non-classical) state toward a coherent (classical) one.

The photon-added coherent state (PACS) after multiple excitation on coherent state can be represented as $|\alpha, m\rangle = \hat{a}^{\dagger m}|\alpha\rangle$ (unnormalized), where $|\alpha\rangle$ is a coherent state of amplitude α, $\hat{a}^{\dagger}$ is the creation operator for the field, and m is a non-negative integer [19]. The state $|\alpha, m\rangle$ is said to be a PACS of order m and amplitude α. The PACS is considered as a state that interpolates between the classical and non-classical states because in the limit of $\alpha \rightarrow 0$, it reduces to the Fock state and in the limit $m \rightarrow 0$ it reduces to the coherent state.

From [19], we can write PACS as

$$|\alpha, m\rangle = k_{\alpha,m}\hat{a}^{\dagger m}|\alpha\rangle, \tag{2.57}$$

where $k_{\alpha,m} = [m!L_m(-|\alpha|^2)]^{-1/2}$ is a normalization factor where $L_m(x)$ is the mth-order Laguerre polynomial and m is an integer.

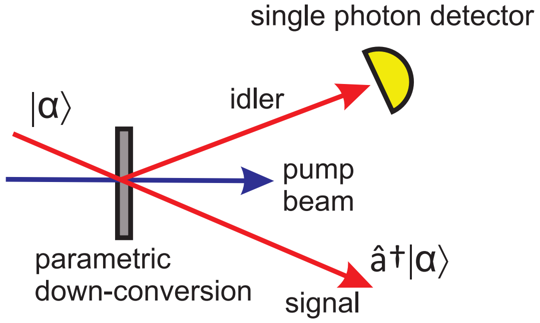

Figure 2.5: The schematic of SPACS. The process is heralded by ”clicks” in single-photon detectors.

In the present work we are concerned with the case when $m = 1$, which corresponds to single photon added coherent states (SPACS) and in other words, we can rewrite Eq. 2.57 as

$$|\alpha, 1\rangle = \frac{\hat{a}^\dagger|\alpha\rangle}{\sqrt{1+|\alpha|^2}} \tag{2.58}$$

and we can further rewrite this equation in Fock basis (using Eq. 2.32) as

$$|\alpha, 1\rangle = \frac{e^{-|\alpha|^2/2}}{\sqrt{1+|\alpha|^2}} \sum_{n=0}^{\infty} \frac{\alpha^n}{\sqrt{n!}} \sqrt{n+1}|n+1\rangle, \tag{2.59}$$

where the absence of the vacuum term is easily noticeable and hence the density matrix element of SPACS are

$$\rho_{i,j}^{|\alpha,1\rangle} = \frac{ij}{\sqrt{i!j!}} \frac{e^{-|\alpha|^2}}{1+|\alpha|^2} \alpha^{i-1} \alpha^{*(j-1)}. \tag{2.60}$$

Non-classicality of SPACS

Using the expression of Wigner function from Eq. 2.47, we can find the expression for the Wigner function of SPACS [2] as

$$W(Z) = \frac{-2(1-|2Z-\alpha|^2)}{\pi(1+|\alpha|^2)} e^{-2|Z-\alpha|^2}, \tag{2.61}$$

where $Z = X + iP$, X and P are the quadratures. $W(Z)$ can clearly become negative under the condition $|2Z - \alpha|^2 < 1$

Mathematical formulation

The state $|\alpha, 1\rangle$ can be written as $\hat{a}^\dagger|\alpha\rangle$ and using Eq. 2.24, we can further write $\hat{a}^\dagger|\alpha\rangle$ in position basis as

$$\hat{a}^\dagger|\alpha\rangle = \hat{a}^\dagger \psi_0(X - \sqrt{2}\alpha), \tag{2.62}$$

where $|\alpha\rangle$ is the input coherent state.

$\hat{a}^\dagger$ can be expressed in terms of $\hat{X}$ and $\hat{P}$ using Eq. (2.13) and then we have

$$\begin{aligned} \hat{a}^\dagger|\alpha\rangle &= \hat{a}^\dagger \psi_0(X - \sqrt{2}\alpha) \\ &= \frac{(X - iP)\psi_0(X - \sqrt{2}\alpha)}{\sqrt{2}} \\ &= \alpha\psi_0(X - \sqrt{2}\alpha) + \frac{(X - \sqrt{2}\alpha) - iP}{\sqrt{2}} \psi_0(X - \sqrt{2}\alpha). \end{aligned} \tag{2.63}$$

In a new displaced co-ordinate frame with $X - \sqrt{2}\alpha = X'$[4] and using this in Eq. 2.63, we have

$$\begin{aligned} \hat{a}^{\dagger}|\alpha\rangle &= \alpha\psi_0(X') + \frac{(X' - iP)}{\sqrt{2}}\psi_0(X') \qquad (2.64) \\ &= \alpha\psi_0(X') + \hat{a}^{\dagger'}\psi_0(X') \\ &= \alpha\psi_0(X') + \psi_1(X'). \end{aligned}$$

Eq. (2.64) is a remarkable result. This implies, SPACS ($\hat{a}^{\dagger}|\alpha\rangle$) is same as displaced superposition of vacuum and single photon fock state ($\alpha|0\rangle + |1\rangle$) or in other words, the Winger function of SPACS is same as Wigner function of ($\alpha|0\rangle + |1\rangle$).

2.3.2 Photon annihilation operator

Unlike the operation of photon addition on coherent state, photon subtraction always leads to classical state because coherent state $|\alpha\rangle$ is an eigen state of annihilation operation ($\hat{a}$) as formulated in Eq. 2.19. However, it is able to convert a Gaussian states into non-Gaussian states [21, 22]. Besides enhancing some of the existing protocols [23, 24], they are able to perform important communication tasks (like entanglement distillation), which are impossible with Gaussian states and operations alone [25, 26].

It is important to note that it is different from conventional deterministic subtraction of objects from an ensemble because it works in a probabilistic way (i.e the probability of taking away a particle from a state is proportional to the number of particles already there, due to $\sqrt{n}$ term in Eq. (2.19)).

Since this is not a unitary process, it is not completely realizable in the lab but it can be approximated as shown before [3, 4, 5].

---

[4] If $X - \sqrt{2}\alpha = X'$ then $dX = dX' \Rightarrow P' = -i\frac{\partial}{\partial X'} = -i\frac{\partial}{\partial X} = P \Rightarrow \hat{a}^{\dagger'} = \frac{X'-P'}{\sqrt{2}} = \frac{X'-P}{\sqrt{2}}$

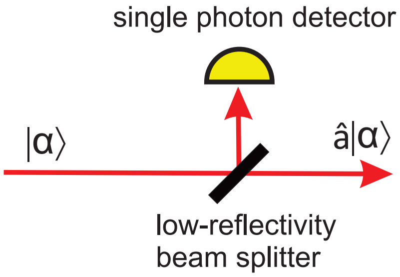

Figure 2.6: The schematic of photon annihilation operation. The process is heralded by ”clicks” in single-photon detectors.

Implementation of the photon annihilation

The action of a beam splitter on quantum states in the signal and trigger input modes described by annihilation operators $\hat{a}_s$ and $\hat{a}_t$ can be modeled as evolution under Hamiltonian [27]

$$\hat{H} = i\lambda\hat{\hbar}a_s\hat{a}_t^\dagger - i\lambda\hbar\hat{a}_s^\dagger\hat{a}_t, \tag{2.65}$$

where λ, assumed real,is related with the amplitude reflectivity of the beam splitter as $r = \sin(\zeta)$ with $\zeta = \lambda\tau/\hbar$ and τ being the fictitious interaction time. If $|r| \ll 1$, the evolution under Hamiltonian (2.65) can be approximated as

$$e^{-i\hat{H}\tau/\hbar} \approx 1 - i\hat{H}\tau/\hbar. \tag{2.66}$$

The beam splitter input consists of the target state $|\alpha\rangle$ in the signal channel and the vacuum state in the trigger channel. The evolution operator, acting on this state, yields

$$e^{-i\hat{H}\tau/\hbar}|\alpha\rangle_s|0\rangle_t \approx |\alpha\rangle_s|0\rangle_t + r\hat{a}_s|\alpha\rangle_s|1\rangle_t. \tag{2.67}$$

Conditioning on single-photon detection in the trigger channel, we obtain state $\hat{a}_s|\alpha\rangle_s$ in the signal. Taylor decomposition (2.66) is valid as long as higher-order terms in its right-hand side can be neglected. This implies $\Pr_{\hat{a}^\dagger} = \alpha^2$.

2.4 Balanced Homodyne Measurement

The quantum theory of the photodetection process has been treated in a number textbooks on quantum optics [7, 29]. The signal produced by a photodiode is – under not too restrictive approximations – found to be proportional to the normally ordered expectation value of the photon number operator $\langle \hat{n} \rangle = \langle \hat{a}^{\dagger}\hat{a} \rangle$. A number of schemes to measure quadrature amplitude instead of the photon number have been discussed in the literature [28, 30], but the most commonly employed scheme is that of balanced homodyne detection.

The balanced homodyne detector (BHD) is a useful tool in quantum optics and quantum information processing with continuous variables (X and P quadratures) [7, 31] since it can be used to measure field quadratures of an electromagnetic mode. These measurements provide information for complete reconstruction of quantum states in the optical domain (optical homodyne tomography).

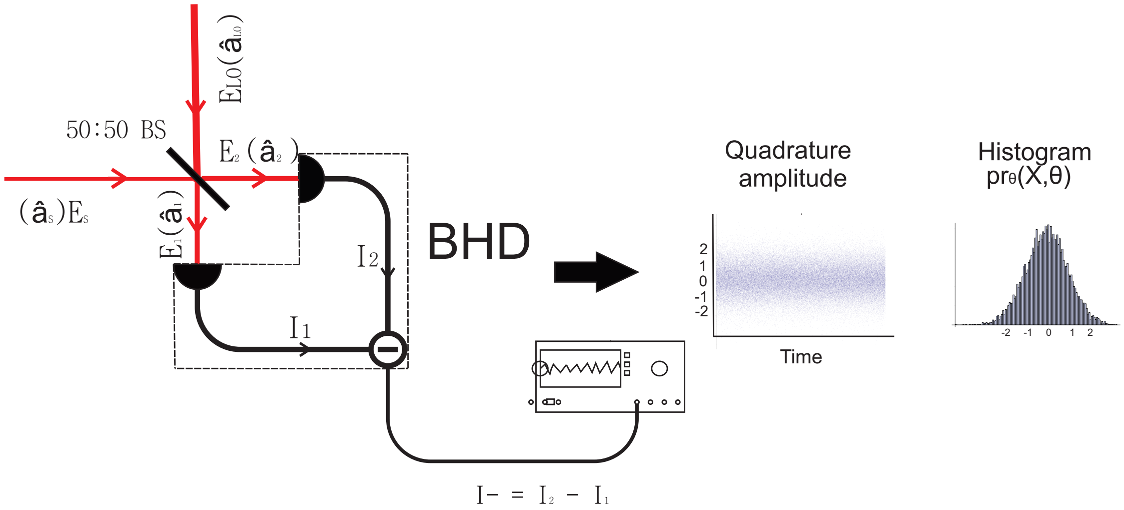

Figure 2.7: Balanced Homodyne Detection (BHD)

The theory of BHD in the optical domain has been discussed quite extensively in literature [7, 32, 28]. From a general point of view, in this scheme a signal, a weak electric field (E_s, treated quantum mechanically) is directed onto a 50:50 beam splitter (BS, shown in Fig. (2.7) in order to be mixed with a second beam, which is going to play the role of a reference beam called local oscillator (LO → E$_{LO}$), shown in Fig. (2.7) — a strong coherent beam (α_{LO}) that can be treated classically. If we assign the mode operators and with these input fields ($\hat{a}_s$ and α_{LO}), the corresponding outputs from the BS (according to the BS transformations) are

$$\begin{aligned}\hat{a}_1 &= \frac{1}{\sqrt{2}}(\hat{a}_s + \alpha_{LO}),\\ \hat{a}_2 &= \frac{1}{\sqrt{2}}(\hat{a}_s - \alpha_{LO}).\end{aligned} \tag{2.68}$$

These annihilation operators are related to the electric field operator associated to each output of the BS. Each output beam is directed to one of the two photodiodes of a homodyne detector (HD). The photocurrents i_1 and i_2 produced by the photodiodes can be assumed to be proportional to the photon numbers of the beams striking each detector:

$$\begin{aligned}\hat{i}_1 \propto \hat{n}_1 &= \hat{a}_1^{\dagger}\hat{a}_1,\\ \hat{i}_2 \propto \hat{n}_2 &= \hat{a}_2^{\dagger}\hat{a}_2.\end{aligned} \tag{2.69}$$

Then, the difference in currents $i_- = i_2 - i_1$ will also be proportional to the difference in photon number

$$i_- \propto \hat{n}_2 - \hat{n}_1 = \alpha_{LO}^{*}\hat{a}_s + \alpha_{LO}\hat{a}_s^{\dagger}. \tag{2.70}$$

If the LO and the signal field originate from the same light source, they have a fixed relative phase θ, that can be controlled (for example with a piezo-electrical controlled mounted mirror). Assuming the zero phase point is chosen so that $\alpha_{LO}$is real, we can re-write the difference photocurrent as:

$$i_- \propto |\alpha_{LO}|(\hat{a}_s e^{-i\theta} + \hat{a}_s^{\dagger}e^{i\theta}). \tag{2.71}$$

By comparing this with Eq. 2.70 we arrive to

$$i_- \propto \hat{n}_- \propto 2^{1/2}|\alpha_{LO}|\hat{X}_\theta = 2^{1/2}\sqrt{N_{LO}}\hat{X}_\theta. \tag{2.72}$$

The difference in photocurrents $i_-$is proportional to the quadrature component $\hat{X}_\theta$. Then, a BHD allows measuring the signal quadrature $\hat{X}_\theta$ (by subtracting the currents produced by the photodiodes), amplified by a factor proportional to the square-root of the intensity of the local oscillator (square root of the average number of photons). The variance in this current will be :

$$\langle \Delta i_-^2 \rangle \propto \langle i_-^2 \rangle - \langle i_- \rangle^2 = 2N_{LO}\langle \Delta \hat{X}_\theta^2 \rangle. \tag{2.73}$$

This means that the variance of the difference photocurrent, which is called shot noise, is linearly proportional to the variance of the quadrature amplitude. This is an important result because classical noise has a different behavior. To see this, if instead of subtracting the currents we add them, we will obtain:

$$i_+ \propto |\alpha|_{LO}|^2 + \hat{a}_s^\dagger \hat{a}_s \approx |\alpha_{LO}|^2 = N_{LO}, \tag{2.74}$$

where we use the fact that the LO is much stronger than the signal. In this case the current is proportional to the average number of photons in the LO, and the quantum feature is lost. The corresponding variance (current noise) is [40]:

$$\langle \Delta i_+^2 \rangle = \langle i_+ \rangle^2 = N_{LO}^2. \tag{2.75}$$

This implies, if we want to measure the quadrature of signal field, we should always measure i_- and not i_+.

The fluctuations of i_- can be recorded as a histogram, and on a proper rescaling, this histogram is essentially the marginal distribution: $\mathrm{pr}(\mathrm{X}_\theta) = \langle \mathrm{X}_\theta | \hat{\rho}_\mathrm{s} | \mathrm{X}_\theta \rangle$, where $\hat{\rho}_s$ is the density operator of the signal field.

2.4.1 Non-ideal behavior of BHD

In real experiments it is impossible to have a perfectly balanced setup and an HD with a perfect subtraction of the classical noise. Optical and electronic components always suffer from issues that prevent them from following the ideal cases; for example, the beam splitters are not perfectly 50:50, the subtraction capability of the HD is limited, the mode matching of the LO and the signal beams is not perfect, the photodiodes had non-unitary quantum efficiency, the presence of electronic noise, etc. Then, in order to give a correct interpretation of the measurements done by the BHD these effects must be taken into account. Here we present a brief discussion of how to take into account the non-ideal behaviors of the electronic noise in the HD when measuring electromagnetic field quadratures and non-ideal behavior due BHD optical setup is discussed in detail in [33]. A more detailed theoretical background can be found in [34, 35, 36, 37, 38, 39].

Drawback of electronic noise in HD

Any non-desirable ambient noises, dark current noises from the photodiodes and the intrinsic noise of the amplifiers fall under the umbrella of electronic noise. The effect of this noise is to add a random quantity $\hat{X}_e$ to the measurement of the field quadrature $\hat{X}_{meas}$. This effect is equivalent to an additional optical loss channel with transmission [38].

$$\eta_e = 1 - \langle \hat{X}_e^2 \rangle / \langle \hat{X}_{meas}^2 \rangle. \tag{2.76}$$

The value of η_e depends not only on the characteristics of the detector, but also on the conditions of the measurement in which the detector is used.

Eq. (2.72) represents the homodyne signal for ideal HD. However, the practical HD has numerous limitations and the relationship between the quadrature measurement and the output current is more complex. It can be approximated by

$$\hat{i}(t) = \hat{i}_e(t) + A \int_{-\infty}^{+\infty} \alpha(t') \hat{X}_\theta(t') r(t - t') dt', \tag{2.77}$$

where $i_e(t)$ is the detector's electronic noise, $\hat{X}_\theta(t')$ is the instantaneous field quadrature value in the signal mode, $\alpha(t')$ and θ are the local oscillator amplitude and phase, respectively and $r(\cdot)$ is its response function. An ideal detector would have $i_e(t) = 0$ and $r(\tau) = \delta(\tau)$. In practice these conditions are not met.

As evident from (2.77), the impact of the electronic noise is minimized by raising the power of the local oscillator and the amplifier gain. However, practical possibilities of increasing the gain without proportionally increasing the electronic noise are limited. The local oscillator power must also be restricted to avoid saturation of the photodiodes and eliminating the classical noise [40]. Therefore in the analysis below we assume A and α to equal their optimal values for the given experimental setting [39].

In order to quantify the effect of electronic noise through η_e, we need to carefully study the response of the detector in the pulsed case regime[5].

Looking back at the equation (2.77) with the pulse width much shorter than the time resolution of the electronics, equation (2.77) takes the form

$$\hat{i}(t) = A\alpha_p \hat{X} r(t) + \hat{i}_e(t), \tag{2.78}$$

where pulse is assumed to occur at $t = 0$, $\hat{X} = \int\limits_{-\infty}^{+\infty} \alpha(t)\hat{X}_\theta(t)\mathrm{d}t/\alpha_\mathrm{p}$ is the normalized quadrature corresponding to the signal mode defined by the shape of the LO and $\alpha_p = \sqrt{\int\limits_{-\infty}^{+\infty} |\alpha(t)|^2 \mathrm{d}t}$ being the effective amplitude of the local oscillator pulse. In other words, neglecting the electronic noise, the shape of the HD response to a single short pulse is given by the detector's response function.

The quadrature measurement is obtained by integrating the homodyne photocurrent over a certain time interval:

$$\hat{X}_\mathrm{meas} = \int\limits_{t_1}^{t_2} \hat{i}(t)\mathrm{d}t = A\alpha_p \hat{X} \int\limits_{t_1}^{t_2} r(t)\mathrm{d}t + \hat{X}_e, \tag{2.79}$$

with

$$\hat{X}_e = \int\limits_{t_1}^{t_2} \hat{i}_e(t)\mathrm{d}t.$$

The optimal choice of the integration limits is determined by the bandwidths of the detector's electronic noise and the temporal width of its response function.

When the local oscillator is a train of pulses with repetition period T, the HD output current

---

[5] When LO is pulsed, which is the case for this thesis.

is given by

$$\hat{i}(t) = A\alpha_p \sum_{j=-\infty}^{\infty} \hat{X}_j r(t - jT) + \hat{i}_e(t), \tag{2.80}$$

where $\hat{X}_j$ is the quadrature operator of the jth pulsed signal mode, with the pulse of interest having index $j = 0$. If the response function is nonzero over an interval longer than T, the quadrature measurement is contaminated by that of the neighboring pulses:

$$\hat{X}_{\text{meas},0} = A\alpha_p \sum_{j=-\infty}^{\infty} R_j \hat{X}_j + \hat{X}_e, \tag{2.81}$$

where $R_j = \int_{t_1}^{t_2} r(t - jT)\mathrm{d}t$. The sum in (2.81) defines a new measured mode whose state is not necessarily identical to that in the $j = 0$th pulsed mode. The corresponding mode matching efficiency (neglecting the electronic noise) is given by

$$\eta_b = \frac{R_0^2}{\sum\limits_{j=-\infty}^{\infty} R_j^2}. \tag{2.82}$$

This efficiency is plotted in Fig. 2.8 for the response function of Gaussian shape as a function of the 3-dB bandwidth of the detector response function spectrum. As we see, a detector bandwidth of at least $0.4/T$ is required for η_b to exceed 99%.

If $r(t)$ is known, so are all R_j and the effect of finite bandwidth can be reversed by means of discrete deconvolution. However, partial reversal can be implemented even if the response function is not known, provided that η_b is sufficiently high, i.e. $|R_j| \ll |R_0|$ for $j \neq 0$, as follows. In a typical detector, R_j are negligibly small for $j > 0$: most of the ringings occur *after* the optical pulse that generates the response. This is the situation, for example, with the detector used in current experiment. Then we have, according to (2.81), and because $\langle \hat{X}_j \hat{X}_k \rangle = \delta_{jk}$ in the vacuum state,

$$\langle \hat{X}_{\text{meas},0} \hat{X}_{\text{meas},i} \rangle = A^2 \alpha_p^2 \sum_j R_j R_{j-i} \approx A^2 \alpha_p^2 R_0 R_{-i}, \tag{2.83}$$

where $\hat{X}_{\text{meas},i}$ denotes the quadrature measurement for the ith pulse. The above correlation can

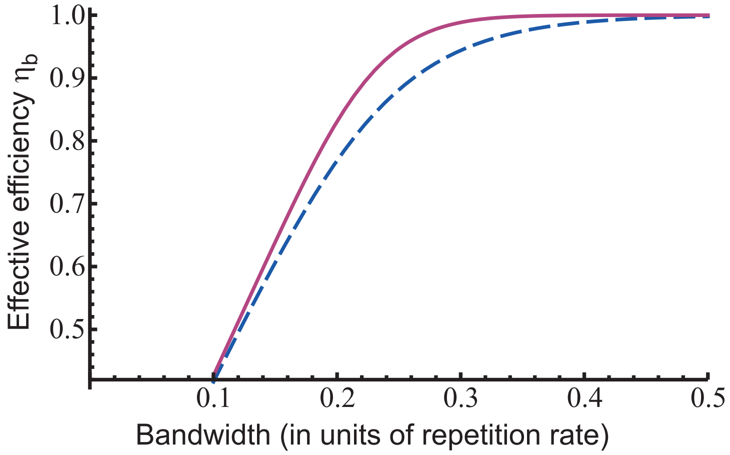

Figure 2.8: Effective efficiency of the HD associated with temporal overlap of responses to different pulsed modes, as a function of the 3-dB bandwidth of the electronics. The response function is assumed Gaussian. The solid line corresponds to a short integration interval $[-\epsilon, +\epsilon]$; the dashed line to the integration interval of length T. Both integration intervals are centered at the peak of the response function.

be easily obtained experimentally, from which one can determine

$$\frac{R_{-i}}{R_0} \approx \frac{\langle \hat{X}_{\mathrm{meas},0}\hat{X}_{\mathrm{meas},i}\rangle}{\langle \hat{X}_{\mathrm{meas},0}\hat{X}_{\mathrm{meas},0}\rangle}. \tag{2.84}$$

One then calculates

$$X'_{\mathrm{meas},0} = X_{\mathrm{meas},0} - \sum_{i=1}^{\infty} \frac{\langle \hat{X}_{\mathrm{meas},0}\hat{X}_{\mathrm{meas},i}\rangle}{\langle \hat{X}_{\mathrm{meas},0}\hat{X}_{\mathrm{meas},0}\rangle} X_{\mathrm{meas},i} \tag{2.85}$$

for each experimentally measured quadrature, thereby eliminating contamination from neighboring pulses. The resulting quadrature values are then renormalized and used in quantum state reconstruction. By means of this technique, the reconstruction efficiency has been improved in Ref. [20].

We now use Wiener-Khinchine theorem[6] to determine the spectral power of the HD output in the pulsed regime. The ensemble average of $i(t)i(t+\tau)$ is a periodic function of time t, hence

---

[6] $S_e(\nu) = \int_{-\infty}^{+\infty} \langle \hat{i}_e(t)\hat{i}_e(t+\tau)\rangle e^{2\pi i\nu\tau}\mathrm{d}\tau$ and $S(\nu) = \int_{-\infty}^{+\infty} \langle \hat{i}(t)\hat{i}(t+\tau)\rangle e^{2\pi i\nu\tau}\mathrm{d}\tau$

we can write

$$\langle \hat{i}(t)\hat{i}(t+\tau)\rangle = \frac{1}{T}(A\alpha_p)^2 \sum_{j,k=-\infty}^{\infty} \langle \hat{X}_j\hat{X}_k\rangle \int\limits_{-T/2}^{T/2} r(t-jT)r(t+\tau-kT)\mathrm{d}t + \langle \hat{i}_e(t)\hat{i}_e(t+\tau)\rangle_t. \tag{2.86}$$

In the vacuum state,

$$\langle \hat{i}(t)\hat{i}(t+\tau)\rangle = \frac{1}{T}(A\alpha_p)^2 \int\limits_{-\infty}^{+\infty} r(t)r(t+\tau)\mathrm{d}t + \langle \hat{i}_e(t)\hat{i}_e(t+\tau)\rangle_t. \tag{2.87}$$

Accordingly,

$$S(\nu) = \frac{1}{T}(A\alpha_p)^2|\tilde{r}(\nu)|^2 + S_e(\nu). \tag{2.88}$$

with

$$\tilde{r}(\nu) = \int\limits_{-\infty}^{+\infty} r(t)e^{2\pi i\nu t}\mathrm{d}t \tag{2.89}$$

being the Fourier image of $r(t)$. In other words, neglecting the electronic noise, the spectrum of the HD output current in the continuous regime is simply the squared amplitude of the Fourier transform of the detector's response function. We see the HD spectrum is determined by the Fourier transform of its response function. When the separation between the pulses is increased, the spectral power reduces proportionally.

The evaluation of the equivalent efficiency (2.76) requires knowledge of $r(t)$; information on the spectra $S(\nu)$ and $S_e(\nu)$ are not sufficient. Let us, however, consider a practically important particular case when the bandwidth of both the detector's response and the electronic noise greatly exceed the laser repetition rate. Suppose the integration in (2.79) is done over the time interval $[-T_0/2, T_0/2]$ with $T_0 < T$. Then we have

$$\langle \hat{X}^2_{\text{meas}}\rangle = \left\langle \left(A\alpha_p\hat{X} \int\limits_{-T_0/2}^{T_0/2} r(t)\mathrm{d}t \right)^2 \right\rangle + \langle \hat{X}_e^2\rangle. \tag{2.90}$$

We assume that the temporal width of the function $r(t)$ is much less than T_0, so the integration limits can be replaced by $\pm\infty$. We then have

$$\langle \hat{X}^2_{\text{meas}}\rangle = (A\alpha_p)^2|\tilde{r}(0)|^2 + \langle \hat{X}_e^2\rangle, \tag{2.91}$$

where

$$\begin{aligned}
X_e &= \left\langle \left(\int\limits_{-T_0/2}^{T_0/2} \hat{i}_e(t)\mathrm{d}t \right)^2 \right\rangle \\
&= \left\langle \int\limits_{-T_0/2}^{T_0/2} \int\limits_{-T_0/2}^{T_0/2} \hat{i}_e(t_1)\hat{i}_e(t_2)\mathrm{d}t_1\mathrm{d}t_2 \right\rangle \\
&= \int\limits_{-T_0/2}^{T_0/2} \int\limits_{-T_0/2-t_1}^{T_0/2-t_1} \langle \hat{i}_e(t_1)\hat{i}_e(t_1+\tau)\rangle \mathrm{d}\tau\mathrm{d}t_1 \\
&\approx \int\limits_{-T_0/2}^{T_0/2} \int\limits_{-\infty}^{+\infty} \langle \hat{i}_e(t_1)\hat{i}_e(t_1+\tau)\rangle \mathrm{d}\tau\mathrm{d}t_1 \\
&= T_0 S_e(0).
\end{aligned} \tag{2.92}$$

Here we again took advantage of the high bandwidth of the electronic noise to modify the integration limits. We also used the fact that the electronic noise $i_e(t)$ is a stationary stochastic process to eliminate the dependence on t_1. Substituting Eqs. (2.88)–(2.92) into (2.76), we find

$$\eta_e = 1 - \frac{T_0}{T}\frac{\hat{S}_e(0)}{S(0)}. \tag{2.93}$$

In other words, the shot-to-electronic-noise clearance measured in the pulsed regime yields a too conservative estimate for the equivalent loss associated with the electronic noise in the high-bandwidth limit. In order to minimize this loss, one needs to choose the integration interval that is as short as possible, but still accommodates the entire detector response function.However, if the detector bandwidth does not greatly exceed the laser repetition rate, we have $T_0 \simeq T$ and the factor of T_0/T in the above equation can be neglected. The exact value for the equivalent loss in this case cannot be determined from the spectra because it depends on the shape of the detector's response function $r(t)$.

2.5 Maximum Likelihood Estimation of Quantum State

The goal of this thesis is to understand Quantum Process Tomography (QPT) of photon addition and subtraction operator[7] but before we proceed there, we need to understand the role of maximum likelihood estimation (MLE) in Quantum state tomography (QST) because of following two reasons: 1. In order to understand the effect of above two processes, it is better to reconstruct the final output state and plot their Wigner function. 2. MLE for state reconstruction will give us an insight into the MLE for QPT in the next section.

2.5.1 Maximum likelihood algorithm

We consider a homodyne tomography experiment performed on an optical mode prepared repeatedly in the same quantum state $\hat{\rho}$. In an experimental run one measures the field quadrature at various phases of the local oscillator. Each measurement is associated with the observables $\hat{X}_\theta$.

For a given phase θ, the probability to detect a particular quadrature value X is given by [41]

$$\mathrm{pr}_\theta(X) = \mathrm{Tr}[\hat{\Pi}(\theta, X)\hat{\rho}_s] \tag{2.94}$$

where $\hat{\Pi}(\theta, X) = |\theta, X\rangle\langle\theta, X|$ is the projector onto this quadrature eigenstate and Tr denotes the trace operation. In the Fock basis, the $(m, n)^{th}$ element of the projection operator is expressed as [41]

$$\Pi_{mn}(\theta, X) = \langle m|\hat{\Pi}(\theta, X)|n\rangle = \langle m|\theta, X\rangle\langle\theta, X|n\rangle \tag{2.95}$$

The homodyne output is analog in nature, but the quadrature samples are obtained after digitizing the signal. One can create N bins by putting the different quadratures acquired at some phase θ_i, in the i^{th} bin ($i \in 1, N$). With the number of quadratures f_i in the ith bin, a histogram can be constructed and would represent the marginal distribution of the ensemble's Wigner

---

[7] Explained in the next section

function at θ_i. However, discretization of continuous experimental data leads to a loss of precision. By reducing the size of a single bin and increasing N, one can limit this loss. Ideally, if M approaches infinity, each bin would be associated to only a single value, i.e. $f_i = 0$ or 1.

Now, if some arbitrarily chosen density matrix $\hat{\rho}$ happens to describe the actual state exceedingly well, then $\mathrm{pr}_{\theta_i}(X_i)|_\rho \rightarrow f_i/N$. If not, a new density matrix needs to be chosen. Then the density matrix needs to maximize the likelihood

$$\mathcal{L}(\rho) = \Pi_i \mathrm{pr}_{\theta_i}(X_i)^{f_i}|_\rho \tag{2.96}$$

in order to describe the measured histograms in the best possible manner. To maximize this likelihood Eq. (2.96), the operator

$$\hat{R}(\hat{\rho}) = \frac{1}{N}\sum_j \frac{f_j}{\mathrm{pr}_j}\hat{\Pi}_j \tag{2.97}$$

is introduced, with $\mathrm{pr}_j \equiv \mathrm{pr}_{\theta_j}(X_j)$ and $\hat{\Pi}_j \equiv \hat{\Pi}(\theta_j, X_j)$ (Eq. (2.94)). We then choose some initial density matrix $\hat{\rho}^0 = \mathcal{N}[\hat{1}]$, and iteratively compute

$$\hat{\rho}^{k+1} = \mathcal{N}[\hat{R}(\hat{\rho}^k)\hat{\rho}^k\hat{R}(\hat{\rho}^k)] \tag{2.98}$$

where $\mathcal{N}$ denotes normalization to a unitary trace and we refer to this scheme as $R\rho R$ algorithm. The convergence of the maximum likelihood procedure as well as a monotonic increment in the likelihood (associated with the density matrix estimate) is assured [41].

2.6 Quantum Process Tomography

Characterization of quantum-dynamical systems is a central task in quantum control and quantum information processing. Knowledge of the state of a quantum system is indispensable in identification and verification of experimental outcomes. In order to fully exploit the capabilities of quantum systems, we need the ability to predict the effect of the quantum systems on an arbitrary input state. This task is especially crucial for verifying the performance of a quantum device in the presence of decoherence. This leads to a quantum version of famous ”black-box” problem and been term as ”Quantum Process Tomography (QPT)”.

QPT has the ability to predict the retrieved quantum state $\mathcal{E}(\rho)$ when the input state ρ is known. QPT is based on the fact that every quantum process (in this case, photon creation and annihilation) is a linear map on the linear space $\mathcal{L}(\mathcal{H})$ of density matrices over the Hilbert space $\mathcal{H}$ on which the process is defined. The associated process can thus be characterized by constructing a spanning set of ”probe” states in $\mathcal{L}(\mathcal{H})$ and subjecting each of them to the action of the quantum black-box. If we measure the process output $\mathcal{E}(\rho_i)$ for a set of density matrices ρ_i of this spanning set, then from linearity relation its effect on $\rho = \sum \gamma_i \rho_i$ would be equal to $\mathcal{E}(\rho)= \sum \gamma_i\ \mathcal{E}(\rho_i)$. Therefore, if ρ_i forms a spanning set within the space $\mathcal{L}(\mathcal{H})$ of linear operators over a particular Hilbert space $\mathcal{H}$, knowledge of $\mathcal{E}(\rho_i)$ is sufficient for extracting complete information about the quantum process.

In this chapter we will talk about the complete characterization of photon creation and annihilation operators.

2.6.1 Coherent state quantum process tomography

This approach has recently been extended to the continuous-variable domain of quantum optics [6]. The reconstruction procedure involves probing the process with coherent states, i.e. simple laser pulses. It relies on the ability of the Glauber-Sudarshan P representation to express the density matrix of any quantum state as a linear combination of coherent states’ density matrices. In this method coherent-state QPT, or csQPT, the role of probe states is played by coherent states [6]. The density operator of an arbitrary state can be written as a linear combination of coherent state density operators using the optical equivalence theorem

$$\hat{\rho} = \int P_{\hat{\rho}}(\alpha)|\alpha\rangle\langle\alpha| d^2\alpha, \tag{2.99}$$

where $P_{\hat{\rho}}(\alpha)$ is the Glauber-Sudarshan P function of state $\hat{\rho}$. Using the linearity of quantum process with respect to density matrices, the process output is then given by

$$\mathcal{E}(\hat{\rho}) = \int P_{\hat{\rho}}\mathcal{E}(|\alpha\rangle\langle\alpha|)d^2\alpha. \tag{2.100}$$

Therefore, if the response of the quantum system to all coherent states are known, the output of any arbitrary unknown quantum state can be computed. In other words, measurements on the set of responses for coherent states provides tomographically complete information about the quantum process. The numerical reconstruction procedures employed in [6, 8] involve an intermediate step of determining the density matrices of the output states $\mathcal{E}(|\alpha\rangle\langle\alpha|)$ for each probe coherent state $|\alpha\rangle$ and subsequent integration with the P function. This approach requires a multi-step calculation and does not guarantee to yield a process that is physically plausible, i.e. completely positive and trace non-increasing.

The method described in the following section does not involve the intermediate step, and reconstructs the process directly from the experimental data using pure statistical inference. The process reconstruction algorithm, on the other hand, is entirely different: it relies on the iterative maximum-likelihood approach. Its major advantage is the possibility to incorporate a *priori* constraints in the reconstruction procedure in order to ensure physically consistent and meaningful results.

Maximum-likelihood methods have been successfully used in the past for quantum state estimation as well as QPT [43, 41, 42]. However, their role in QPT has been limited to the discrete variable state space. The technique presented in this chapter extends the purview of maximum-likelihood QPT to the continuous variable state space, thereby allowing physically consistent quantum process estimation through homodyne tomography experiments [31].

2.6.2 Maximum likelihood estimation

The scheme[8] used here is an iterative process estimation using Jamiolkowski isomorphism and is based on the application of a maximum-likelihood based QPT scheme [43, 31] to quadrature measurements in the Hilbert space associated with a harmonic oscillator. Consider a quantum optical process $\mathcal{E}$ acting upon an optical mode prepared in some quantum state $\hat{\rho}_m$. The positivity of density matrices deems it necessary that $\mathcal{E}$ be a completely positive (CP) map, in addition to being trace non-increasing [42]. The output state $\mathcal{E}(\hat{\rho}_m)$ of such a process can be subjected to optical homodyne measurements of its field quadratures in X_θ (Eq. (2.43)). The probability of detecting a specific quadrature value X for a phase θ (2.94).

$$\mathrm{pr}_\theta^m(X) = \mathrm{Tr}[\hat{\Pi}(\theta, X)\mathcal{E}(\hat{\rho}_m)], \tag{2.101}$$

where $\hat{\Pi}(\theta, X) = |\theta, X\rangle\langle\theta, X|$ is the projector associated with the quadrature eigenstate $|\theta, X\rangle$. The above expression can be considered as a probability distribution function with ε as the parameter. If one performs N measurements for each of the M input probe states $\hat{\rho}_m$, obtained as a set of phase and corresponding quadratures values $\{\theta_{i,m}, X_{i,m}\}$ where $1 \leq i \leq N$ and $1 \leq m \leq M$, one can obtain the log-likelihood functional as

$$\begin{aligned} \mathcal{L}(\mathcal{E}) &= \sum_{m,i} \ln(\mathrm{pr}_{\theta_{i,m}}^m(X_{i,m})); \qquad (2.102) \\ &= \sum_{m,i} \ln(\mathrm{Tr}[\hat{\Pi}(\theta_{i,m}, X_{i,m})\mathcal{E}(\hat{\rho}_m)]). \end{aligned}$$

The goal of maximum-likelihood estimation is to determine the parameter $\mathcal{E}_{est}$ that is as close to the actual parameter as possible, by maximizing the likelihood function $\mathcal{L}(\mathcal{E})$ over the space of CP maps

$$\mathcal{E}_{est} = \arg\max_{\mathcal{E}} \mathcal{L}(\mathcal{E}). \tag{2.103}$$

This optimization problem is not straightforward and has been handled through a technically simpler approach involving the formulation of an extremal equation that maximizes the log-likelihood function given in equation (2.102).

---

[8] This work is based on [9] with Author's permission

Basis selection

Any arbitrary quantum state ρ can be expressed in the Fock representation as

$$\rho = \sum_{m,n=0}^{\infty} \rho_{mn}|m\rangle\langle n|. \tag{2.104}$$

Subjecting this to an unknown process $\mathcal{E}$, and imposing linearity yields

$$\varepsilon(\rho) = \sum_{j,k,m,n=0}^{\infty} \varepsilon_{jk}^{mn}\rho_{mn}|j\rangle\langle k|, \tag{2.105}$$

where

$$\varepsilon_{jk}^{mn} := \langle j|\varepsilon(|m\rangle\langle n|)|k\rangle, \tag{2.106}$$

is a rank-4 tensor, hereafter referred to as the 'process tensor (superoperator)'. Thus by expressing input and output states in the Fock basis, a quantum process can be uniquely represented and characterized by its rank-4 tensor, which relates the matrix elements of the output and input states according to

$$[\rho_{out}]_{jk} = \sum_{m,n,j,k} \varepsilon_{jk}^{mn}[\rho_{in}]_{mn}. \tag{2.107}$$

This implies, the goal of csQPT in Fock basis is to estimate ε_{jk}^{mn}

Optimization of $\mathcal{E}$

The projectors $\hat{\Pi}(\theta, X)$ can be expressed in this basis as (2.95)

$$\Pi_{mn}(\theta, X) = \langle m|\Pi(\theta, X)|n\rangle = \langle m|\theta, X\rangle\langle\theta, X|n\rangle, \tag{2.108}$$

where the overlap of the quadrature eigenstate with the number state is given by [41]

$$\langle m|\theta, X\rangle = e^{im\theta}\left(\frac{1}{\pi^{1/4}}\right)\frac{H_m(X)}{\sqrt{2^m m!}}e^{-X^2}. \tag{2.109}$$

Using Jamiolkowski isomorphism between linear CP maps $\mathcal{E}$ from operators on the Hilbert space $\mathcal{H}$ to the space $\mathcal{K}$ and positive semidefinite operators $\hat{E}$ on the Hilbert space $\mathcal{H} \otimes \mathcal{K}$, the explicit relation between $\hat{E}$ and $\mathcal{E}$ is given as [44]

$$\hat{E} = \sum_{m,n,j,k} \mathcal{E}_{jk}^{mn}\, |m\rangle\, \langle n| \otimes |j\rangle\, \langle k|\,. \tag{2.110}$$

With this definition, the output $\hat{\rho}_{\text{out}} \in \mathcal{K}$ of a process for an input state $\hat{\rho}_{\text{in}} \in \mathcal{H}$ is

$$\hat{\rho}_{\text{out}} = \mathcal{E}(\hat{\rho}_{\text{in}}) = \text{Tr}_{\mathcal{H}}\left[\hat{E}\left(\hat{\rho}_{\text{in}}^{T} \otimes \hat{I}_{\mathcal{K}}\right)\right], \tag{2.111}$$

where T denotes transposition in the number basis. With trace preserving condition ($\text{Tr}[\hat{\rho}_{\text{out}}] = \text{Tr}[\hat{\rho}_{\text{in}}]$) over the process $\mathcal{E}$, one obtains

$$\text{Tr}_{\mathcal{K}}[\hat{E}] = \hat{I}_{\mathcal{H}}. \tag{2.112}$$

The problem has thus reduced to the determination of $(\text{dim}\mathcal{H}\text{dim}\mathcal{K})^2$ parameters subject to $\text{dim}\mathcal{H}^2$ constraints. When the input and output Hilbert spaces are identical, this amounts to evaluating $\text{dim}\mathcal{H}^4 - \text{dim}\mathcal{H}^2$ free parameters.

For the process output of the input probe state $\hat{\rho}_m$, the probability of reading a quadrature value X for a given local oscillator phase θ can be obtained by substituting (2.111) into equation (2.101) to obtain

$$\text{pr}_{\theta}^{m}(X) = \text{Tr}\left[\hat{E}\left(\hat{\rho}_{m}^{T} \otimes \hat{\Pi}(\theta, X)\right)\right]. \tag{2.113}$$

In order to stand as the most likely quantum process that has the set of outcomes $\{\theta_{i,m}, X_{i,m}\}$ for the input probes $\{\hat{\rho}_m\}$, rank-4 tensor $\hat{E}$ should then maximize a constrained log-likelihood functional. The relevant log-likelihood functional is given as

$$\begin{aligned} \mathcal{L}(\hat{E}) &= \sum_{m,i} \ln\left(\text{pr}_{\theta_{\text{i,m}}}^{\text{m}}(\text{X}_{\text{i,m}})\right) - \text{Tr}[\hat{\Lambda}\hat{E}] \\ &= \sum_{m,i} \ln\left(\text{Tr}\left[\hat{E}\hat{\rho}_{m}^{T} \otimes \hat{\Pi}(\theta_{i,m}, X_{i,m})\right]\right) - \text{Tr}[\hat{\Lambda}\hat{E}], \end{aligned} \tag{2.114}$$

where $\hat{\Lambda} = \hat{\lambda} \otimes \hat{I}_{\mathcal{K}}$ and $\hat{\lambda}$ is the Hermitian matrix of Lagrange multipliers that incorporates the trace preservation condition (2.112). An extremal equation can be obtained by varying equation (2.114) with respect to $\hat{E}$:

$$\delta\mathcal{L}(\hat{E}) = \mathcal{L}(\hat{E} + \delta\hat{E}) - \mathcal{L}(\hat{E}) = 0, \tag{2.115}$$

which gives

$$\text{Tr}\left[\left(\sum_{m,i} \frac{1}{p_{\theta_{i,m}}^{m}(x_{i,m})}\hat{\rho}_{m}^{T} \otimes \hat{\Pi}(\theta_{i,m}, X_{i,m}) - \hat{\Lambda}\right)\delta\hat{E}\right] = 0. \tag{2.116}$$

This holds for all $\delta\hat{E}$, so that the expression in the parentheses can be equated to zero and one has

$$\hat{E} = \hat{\Lambda}^{-1}\hat{R}\hat{E}, \tag{2.117}$$

where

$$\hat{R} = \sum_{m,i} \frac{1}{p^{m}_{\theta_{i,m}}(x_{i,m})}\hat{\rho}^{T}_{m} \otimes \hat{\Pi}(\theta_{i,m}, x_{i,m}). \tag{2.118}$$

Eq. (2.117) can be rewritten as $\hat{E} = \hat{E}\hat{R}\hat{\Lambda}^{-1}$ (Hermicity). Using this, along with equation (2.117), we arrive at

$$\hat{E} = \hat{\Lambda}^{-1}\hat{R}\hat{E}\hat{R}\hat{\Lambda}^{-1}. \tag{2.119}$$

$\hat{\Lambda}$ can be determined by substituting the expression for $\hat{E}$ in equation (2.119) into the trace-preservation condition (2.112):

$$\hat{\lambda} = \left(\mathrm{Tr}_{\mathcal{K}}[\hat{R}\hat{E}\hat{R}]\right)^{1/2}. \tag{2.120}$$

Equations (2.119) and (2.120) can be solved numerically through iterations, starting from an unbiased initial $\hat{E}$, such as $\hat{E}^{(0)} = \hat{I}_{\mathcal{H}\otimes\mathcal{K}}/(\dim\mathcal{K})$. At each step of the iterations, the positive semi-definiteness of $\hat{E}$ is ensured and the constraint $\mathrm{Tr}_{\mathcal{K}}[\hat{E}] = \hat{I}_{\mathcal{H}}$ is satisfied.

Trace non-preserving processes

Quantum processes may also be probabilistic, in which case the trace of the input quantum state is not preserved. The probability of occurrence of a probabilistic quantum process is given by

$$p_{\text{success}} = \mathrm{Tr}[\mathcal{E}(\hat{\rho})]. \tag{2.121}$$

The reconstruction of probabilistic quantum processes can be viewed as a reconstruction of a trace-preserving, deterministic CP map $\tilde{\mathcal{E}}$ if the failure of the process is taken to be a measurement event associated with the projection operator $\hat{\Pi}_{\emptyset}$ onto a fictitious state $|\emptyset\rangle$ [44]. In order to analyze such a process, one can extend the Hilbert space to form $\mathcal{K}_{\text{total}} = \mathcal{K} \oplus \mathcal{K}_{\text{fail}}$, where $\mathcal{K}_{\text{fail}}$ is spanned by the single state $|\emptyset\rangle$. The original set of projectors $\hat{\Pi}_{\theta}(x)$ for each θ is augmented by adding $\hat{\Pi}_{\emptyset}$ so that the new set of projectors satisfies the closure relation over

$\mathcal{K}_{\text{total}}$, i.e. $\forall\theta \int \hat{\Pi}_\theta(x)dx + \hat{\Pi}_\emptyset = I$. Subsequently, the likelihood function, with the extended trace-preserving map $\tilde{\mathcal{E}}$ as parameter, can be rewritten as

$$\mathcal{L}(\hat{\hat{E}}) = \sum_{m,i} \left[g_m \ln\left(p^m_{\theta_{i,m}}(x_{i,m})\right) + (1 - g_m)\ln\left(p^m_\emptyset\right)\right] - \mathrm{Tr}[\hat{\Lambda}\hat{\hat{E}}], \tag{2.122}$$

where g_m is the fraction of successful events over total events, which can be determined experimentally. The extremal equation would then contain a modified operator $\hat{R}$ given by

$$\hat{\hat{R}} = \sum_{m,i} \left[\frac{g_m}{p^m_{\theta_{i,m}}(x_{i,m})} \hat{\rho}^T_m \otimes \hat{\Pi}(\theta_{i,m}, x_{i,m}) + \frac{1 - g_m}{p^m_\emptyset} \hat{\rho}^T_m \otimes \hat{\Pi}_\emptyset \right]. \tag{2.123}$$

Iterations can now be performed with the new $\hat{\hat{R}}$ to obtain the trace-preserving process tensor $\hat{\hat{E}}$. The actual process tensor $\hat{E}$ is obtained by taking the projection of the estimated tensor $\hat{\hat{E}}$ onto the subspace $\mathcal{H} \otimes \mathcal{K}$.

2.6.3 Practical issues

- The first issue is associated with the infinite dimension of optical Hilbert space. In practical implementation of csQPT, the process tensor is reconstructed for a subspace $\mathcal{H}(n_{max})$ of the Hilbert space spanned by Fock states up to a certain cut-off value, n_{max}. The choice of n_{max} is correlated with the maximum amplitude α_{max} of the set of coherent probe states. The $\mathcal{H}(n_{max})$ should be chosen such that it accommodates all the coherent state and the associated output states. Otherwise, we will have something called *truncation error* because of inadequately chosen $\mathcal{H}(n_{max})$. However, a high cut-off value may give rise to another class of inaccuracies, which we call *data insufficiency errors* [9]. In contrast to the truncation errors, the data insufficiency errors grow with n_{max}, but only apply to the process tensor elements associated with high input photon numbers. So, in order for this algorithm to work for our purposes, we need to follow a dual-step procedure for the choice of the cut-off. The initial value of n_{max} must be sufficiently high to ensure absence of truncation errors. Subsequently, after the iterative cycle has been completed, we choose a secondary cut-off value, $n^{'}_{max} \leq n_{max}$, and remove all the process tensor elements containing indices above $n^{'}_{max}$. The choice of $n^{'}_{max}$ can be determined by calculating the statistical errors associated with each process tensor element [44].

- Optical losses and inefficient detectors - the algorithm we used for estimation automatically permits the correction for optical loss or detector inefficiency. In order to account for non-unitary efficiency η, the projectors are replaced by

$$\hat{\Pi}_{\eta}(\theta, x) = \sum_{m,n,j,k} B_{n+k,n}(\eta) B_{m+k,m}(\eta) \langle m|\hat{\Pi}(\theta, x)|n\rangle \times |m+k\rangle\langle n+k|, \tag{2.124}$$

  where $B_{n+k,n} = \left[\binom{n+k}{k}\eta^{n}(1-\eta)^{k}\right]^{1/2}$. Substituting this into equation (2.118) and performing the iterations generates the original process tensor pertaining to the case of ideal detection.

- Many physically relevant processes are phase-invariant: applying an optical phase shift to the input state results in the same shift to the output. Mathematically, such processes satisfy the following relation [8, 41]

$$\varepsilon[\hat{U}(\phi)\hat{\rho}\hat{U}^{\dagger}(\phi)] = \hat{U}(\phi)\varepsilon(\hat{\rho})\hat{U}^{\dagger}(\phi). \tag{2.125}$$

  If the action of the process on a coherent state $|\alpha\rangle$ is known, so is the outcome for $|\alpha e^{i\phi}\rangle$. Therefore, one needs to only perform measurements for input coherent states with amplitudes on the positive real axis. When condition (2.125) is applied in the Fock basis, the elements of the process tensor $\mathcal{E}^{mn}_{jk}$ for a phase-invariant process vanish except when $m - n = j - k$.

- In some cases, the value of the log-likelihood oscillates before converging to the maximum owing to overshoots. Stabilization can be achieved using the diluted algorithm that slows down but guarantees convergence [51]. The operator $\hat{R}$, in that case, is modified to a weighted sum of itself and the identity operator as

$$\hat{R}' = (1-\mu)\hat{R} + \mu\hat{I}, \tag{2.126}$$

where $0 \leq \mu \leq 1$. As the value of μ increases, the algorithm becomes more and more dilute, resulting in increased stability but a reduced rate of convergence. One may try to find the optimal value of μ that maximizes the increase in likelihood at the cost of increased computational complexity. Gradually varying the value of μ during the iterations may be justified for some processes.

Chapter 3

Experiment

So far we have talked about the underlying concepts behind quantum process tomography (QPT) of photon addition and subtraction without talking about its experimental implementation. In this chapter, we will see its implementation using a mode-locked Ti:Sapphire laser, which emits transform-limited pulses[1] at ~790 nm with a repetition rate of 76 MHz and a pulse width of ~1.7 ps.

3.1 Optical Components

3.1.1 Light source

In order to perform QPT, we need to generate single-photon wave packets in a well controlled fashion and that calls for a numerous limitation on the choice of the light source.

The primary light source used in our experiment is a mode-locked Ti:Sapphire laser (Coherent MIRA 900) with its cavity configured so as to obtain transform-limited pulses with a time duration τ_p (full width at half maximum) around 1.7 ps. The pulses were separated by 13.1 ns, implying a repetition rate $f_{rep} \sim 76$ MHz. Central wavelength (λ_c) was adjusted around 791.0 nm, and the spectral line width $\Delta\lambda$ was usually between 0.6 and 0.7 nm - measured using Pulse Scope autocorrelator and spectrometer.

The MIRA was pumped by a Verdi V-10 laser, which generated roughly 10.0 W of power[2] at 532 nm in continuous wave (CW) mode. The output power from MIRA was ~ 1.7 W with horizontal polarization and in a TEM00 mode.

---

[1] signifies a pulse that is as short as its spectral bandwidth allows it to be. In other words, the minimum time-bandwidth product is achieved.

[2] All power refers to the *average* power, unless mentioned otherwise.

Characteristics and requirements of the laser

- Pulse laser implies higher peak power for non-linear process such as second harmonic generation (SHG) and spontaneous parametric down conversion (SPDC).
- Pulse width broader than 10 ps will result into lower peak intensity and pulse width of the order of fs can lead to the distortion of the SHG pulse due to group-velocity mismatch [49].
- The repetition should not exceed the time resolution of the detection system, implying detector bandwidth $\geq f_{rep}$.
- In order to perform experiments, there should be detectors available at λ_c.

3.1.2 Non-linear crystals

Lithium triborate crystal

In order to generate second harmonic at $\lambda = 395.5$ nm as described in section 2.2, we used Lithium Triborate (LBO) crystal with following specifications.

- Dimension: Length = 17 mm and Width = Height = 2 mm.
- Cut at $\theta = 90°, \phi = 32.7°$ for phase matching with the pre-decided incoming beam.
- Anti-reflection coating both at 790 nm and 395 nm.
- Type I phase-matching.

Periodically poled potassisum-titanyl phosphate crystal

We used periodically poled potassisum-titanyl phosphate crystal (PPKTP) crystal for SPDC as described in section 2.2. The crystal has following specifications.

- Dimension: Length = Width = 2 mm and Height = 1 mm.
- Poling period: $\sim 9\ \mu$m.

3.1.3 Optical detectors

Homodyne detector

We talked about the requirement of homodyne detector (HD) for quadrature measurement in section 2.4 and here we will see some of the characteristics of the HD used in the experiment [39].

Some of the important features a HD should have in order to be used in our experiment are:

- High bandwidth and a flat amplification profile within that bandwidth - The *high bandwidth* requirement comes from the fact that a HD must be able to measure the field quadratures with sufficient time resolution. It must also feature a *flat amplification profile* otherwise the response of HD to each individual pulse will exhibit ringing, which degrade the detector's time resolution and distort the measurement
- High ratio of the measured quantum noise over the electronic noise - Any non-desirable ambient noises, dark current noises from the photodiodes and the intrinsic noise of the amplifiers fall under the umbrella of electronic noise, discussed in equation 2.76.
- High common mode rejection ratio (CMRR) - A HD must have a high subtraction capability between the two photocurrents produced by the photodiodes. This can be expressed as a generalized common mode rejection ratio (CMRR) of the balanced detection [46, 39]. The CMRR measures the ability of the device to reject the classical noise of the local oscillator [47, 40]. High CMRR is difficult to achieve because the response functions of the photodiodes are not exactly the same. Therefore a pair of photodiodes with response functions as similar as possible must be chosen.
- Quantum efficiency of the photodiodes - The quantum efficiency, η_{det}, is the probability of the incoming light being converted to measurable signal. In the other words, it is a quantity defined for a photosensitive device such as photodetector as the percentage of

photons hitting the photoreactive surface that will produce an electron and hole pair, that is

$$\text{rate of signal pulses} = \eta_{det}\,\text{rate of photons}. \tag{3.1}$$

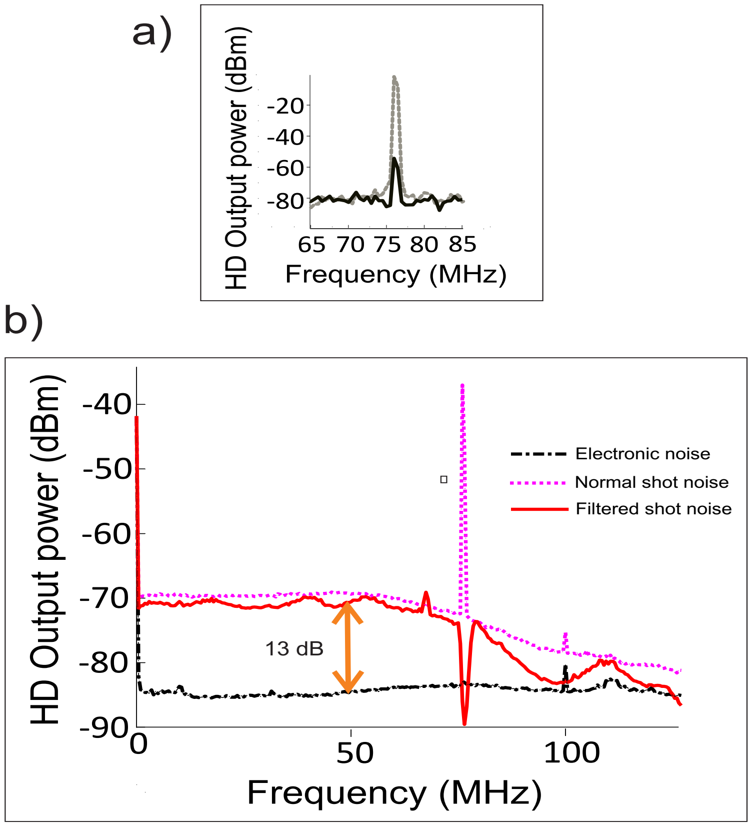

Figure 3.1: a) Response of HD at 100 μW of local oscillator (LO) power, necessary to calculate CMRR. Grey (top) trace: one photodiode blocked; Black (bottom): both photodiode illuminated. b) Spectral response of HD at 12 mW of LO power. The large peak is a laser repetition rate. Pink (top): LO Shot noise without any filter; Red (middle): LO shot noise with notch filter; Black (bottom): Electronic/Dark current noise - as seen on the spectrum analyzer.

While keeping the above criteria in mind, we used the HD with following specifications.

- Wavelength of operation - 791.0 nm.

- 3 dB bandwidth - 100 MHz.
- CMRR - 52.4 dB.
- Clearance - 13 dB.
- Photo diode - Matched pair of S5972 Hamamatsu photodiodes with quantum efficiency of 91% at λ = 780 nm and a high cut-off frequency (500 MHz) when the supplied in a 12 V reverse voltage configuration.

The detector was suitably chosen for our requirement and has been discussed in detail in Kumar *et. al* [39].

Single photon counting module

In order to herald the single photon in the trigger channel, we used a commercially available Silicon avalanche photo diode single photon counting module (SPCM) from PerkinElmer (SPCM-AQR-14-FC), that features a fiber-optic receptacle pre-aligned to the optical detection system. It has a quantum efficiency (η_{spcm}) around 55% at 790 nm and a dark count rate of $\leq$ 100 Cts/s. With a detection of a photon, a 30 ns wide TTL pulse of $\geq$ 2.5 V is obtained at the output, that has a 50 Ω load termination.

One major reason for using a fiber-coupled module is that direct (space-coupled) detectors have a poor mode selectivity, i.e. by accepting photons from numerous spatial, temporal and polarization modes, they do not provide any means to measure photon statistics restricted to a single mode. In contrast, a single mode fiber (with pre-chosen characteristics) acts as an efficient spatial filter before the SPCM. In our experiment, we use a patch-cord (SMJ-3A3A-780-5/125-3-3APC, from OZ Optics) and first couple the seed beam into this fiber, for reasons explained in [18].

3.2 Single Photon Source

In our experimental realization of quantum process tomography of photon addition and subtraction, the first crucial steps are to generate single photon added coherent state (SPACS) and single photon subtracted state. The second part is rather easy to implement experimentally as compared to the first part because SPACS requires a reliable and efficient single photon source unlike photon subtraction (see section 2.3). This calls for a complete description of a single photon source.

Our goal is to generate a single photons at λ = 791.0 nm such that it can be added to a coherent state (probe field) in the same spatial mode and in order to achieve this we used SPDC to convert the photons at λ = 395.5 nm into daughter photons pairs at λ = 791.0 nm as described in section 2.2.

3.2.1 Second harmonic generation

We took a portion of the pulsed laser from MIRA ($\approx$ 1.5 W, vertical polarization) as shown in the Fig. 3.2 with the help of HWP1 and PBS1 and then directed toward LBO crystal, which gave us $\sim$ 250 mW of λ 395.5 nm pump beam ($\eta_{LBOconversion} \approx 20\%$).

The crystal was kept on a combination of translational and angular stage (not shown in Fig. 3.2), where we had the option of changing the horizontal and angular orientation of the crystal. In conjunction with this stage, we uses an in-coupling lens of 100 mm (L1) to focus the light into the LBO, yielding a Rayleigh length that satisfies the Boyd-Kleinmann relation [48], giving the best second harmonic generation [50, 49].

We further clean the mode using a combination of spectral filters (F1) at 395.5 nm (to eliminate the unused input light due to poor efficiency of LBO), pin-hole (P1) and Iris (I1) as shown in the Fig. 3.2. Eventually, we obtained $\sim$ 90 mW of 395.5 nm TEM00 mode beam, which acted as the pump beam for SPDC.

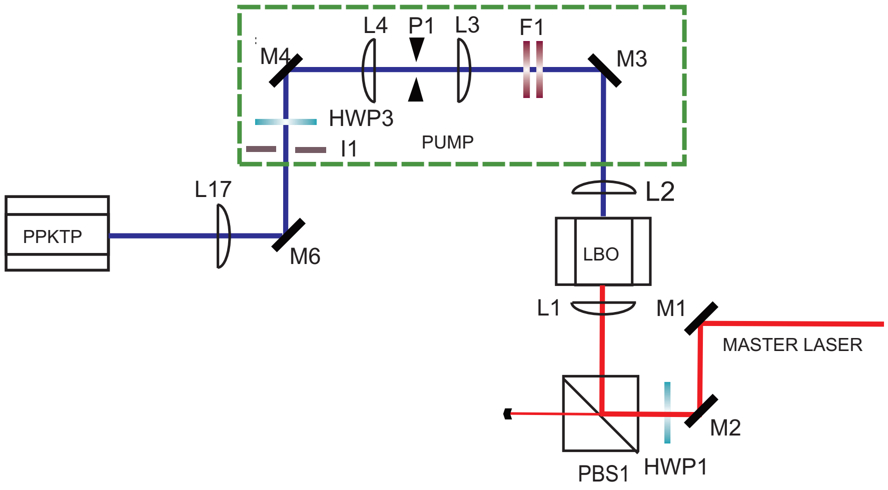

Figure 3.2: Generation of SHG from laser pump beam for PPKTP crystal using SHG inside LBO.

3.2.2 Preparation of PPKTP for SPDC

We used the SHG generated (~ 90 mW) from LBO to pump the PPKTP for SPDC and 2 mm long PPKTP crystal results in to moderate conversion efficiency. However, this conversion is not good enough to observe the down-converted photons on camera for alignment purposes. So, we chose an alternative method to align the crystal using a dummy optical beam called *Seed*. Using Seed we generated a dummy signal (DFG: difference frequency generation), which emulated the single photon for alignment purposes.

Seed beam

We took a portion of incoming beam of power ~ 6 mW from MIRA using PBS2 and HWP2 (shown in figure 3.3) and called it Seed.

Seed was used to generate DFG, which helped mode-matching the LO with the *future* single photon.

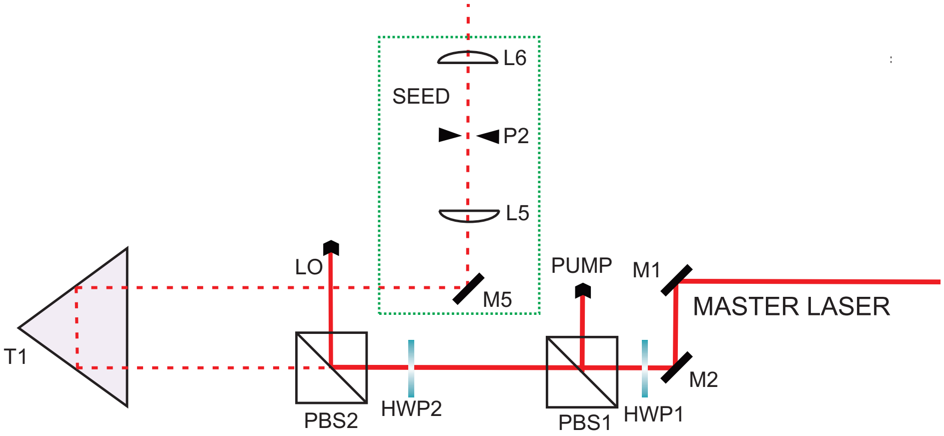

Figure 3.3: Seed beam.

Mode matching of the seed and pump beam

To ensure a good DFG beam, and consequently a good production efficiency of parametrically down-converted photons, we need to mode-match the seed beam to the pump beam, in this way we can find the optimal phase matching conditions of the PPKTP crystal. We perform the mode-matching on a camera (not shown in the figure) using mirrors M4 and M6 [33] (shown in figure 3.7).

SHG from seed

In order to optimize the phase-matching of PPKTP, we changed the polarization of the seed beam using HWP5 (shown in figure 3.7) and optimized the second harmonic generation from PPKTP by changing the orientation and temperature of the crystal. Typically we observed $\sim 1\mu$W SHG for the optimized configuration and this method works because both pump and seed have the same spatial characteristics [18, 50]. Once the crystal is phase-matched, we changed the polarization back to its original configuration to used later for difference frequency generation (DFG).

Difference frequency generation

It is described as the three-wave processes of differencing frequencies between the pump and seed, i.e. $\omega_{DFG} = \omega_{pump} - \omega_{seed}$. The signal and idler modes were initially assumed to be vacuum before the nonlinear interaction; instead, if a coherent beam (seed) is injected in the idler mode along with the pump beam, the spontaneous down conversion process is replaced by a stimulated one [48] (Fig. 3.4). Then, due to the difference frequency generation process (DFG), a macroscopic amount of light is produced in the signal mode, which allows an easier alignment and matching with the LO beam through the adjustment of parameters such as beam direction, divergence, spatial and temporal width and optical delay. The phase matching conditions of the process also will produce the two beams to have opposite polarizations, while the undepleted seed beam propagates along the path of the trigger, the DFG will propagate through the signal channel.

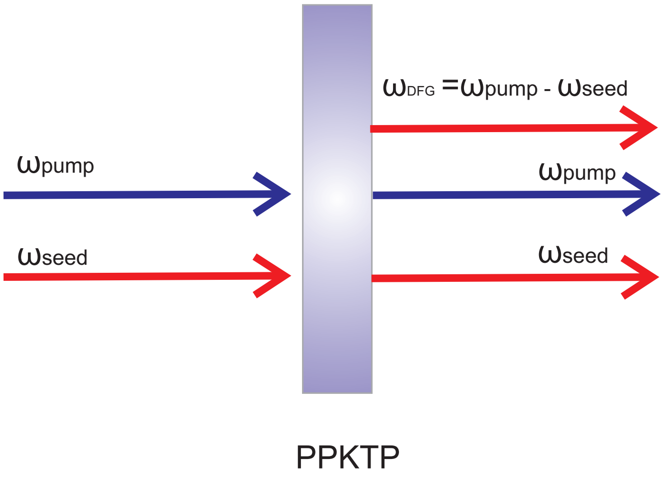

Figure 3.4: Difference frequency degeneration inside PPKTP crystal.

3.2.3 Difference frequency generation (DFG) alignment

Generation of DFG also guarantees the phase matching of PPKTP crystal with the incoming pump beam for parametric down conversion. The generated DFG can be monitored by placing temporarily a beam splitter (BSD) after HWP8 to deflect the beam to a photodiode (PD) and a web cam (C1), shown in the Fig. 3.5. The spatial mode of the DFG should be as Gaussian as possible and this can be improved by adjusting the orientation of the PPKTP crystal mount. To avoid leakage of the remaining seed beam into the signal channel, the orientation of the half wave plate (HWP6) and the quarter wave plate (QWP1) are changed to minimize the interference produced by the DFG and the seed as seen in the photodiode (PD) placed after BSD. The final DFG observed was usually around ~70μW. LO must be blocked during this time.

3.2.4 DFG and LO mode-matching

The characteristics of the DFG beam are critical to the overall success of the experiment due to its implications on the down-conversion amplitude and down-conversion modes. Furthermore, a good match of the DFG with the LO entails a higher efficiency of the homodyne detection.

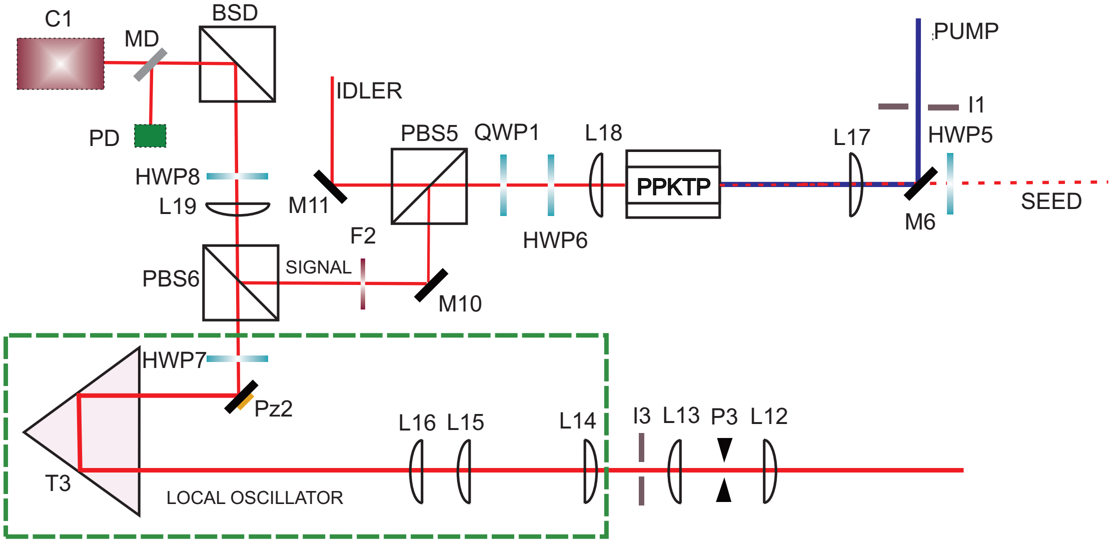

Figure 3.5: Mode-matching between LO and DFG.

To improve the mode-match of the DFG with the LO (now opened), they must be projected on a web cam (C1) and photodiode (PD), shown in figure 3.5. First the power of the LO must be equalized to the DFG one by using the HWP7 and PBS6. Then, the spatial position of the two beams can be overlapped by adjusting the mounted mirror (M10) and PBS6 [33]. We typically worked with the interference visibility of ≥ 92%.

3.2.5 Trigger channel

In order to align the trigger channel, we used seed to emulate the down-converted idler photon in the trigger channel. The seed polarization is chosen horizontal after QWP1 quarter wave plate as shown in Fig. 3.6. We couple the incoming seed into optical fiber with the help of mirrors M12 and M13 as well as fiber coupling stage (FC), the trigger beam waist can be changed using lenses L20 and L21. We routinely observed a coupling efficiency of ∼ 80 %.

In order to remove the unused pump beam after inefficient PDC, we uses an optical filter (F3) of band width 10 nm and optical filter (F4) of bandwidth 0.3 nm with center wavelength as 791.0 nm - shown in figure 3.6.

We use a SMJ-3A3A-780-5/125-3-3APC single mode fiber from OZ Optics.

After the alignment is done, the seed beam is blocked and the fiber is connected to the SPCM, where TTL pulse from SPCM is the trigger signal for the digital oscilloscope and HD.

3.2.6 BHD alignment

In order to perform BHD, we take our signal and local oscillator (LO) from the same source, where local oscillator is always horizontally polarized and signal is always vertically polarized. We then combine them on Polarizing Beam Splitter (PBS7) followed by a Half-Wave Plate (HWP8), which act as a ”variable beam splitter” (shown in figure 3.7) and in this way we can balance the power in the arms of the interferometer to produce response functions as similar as possible in the photodiodes of the HD (in the time domain, this means making the photodiodes produce similar peak-to-peak values and pulse shapes; in the spectral response corresponds to a reduction in the power of the repetition rate and its harmonics). In addition to a combination

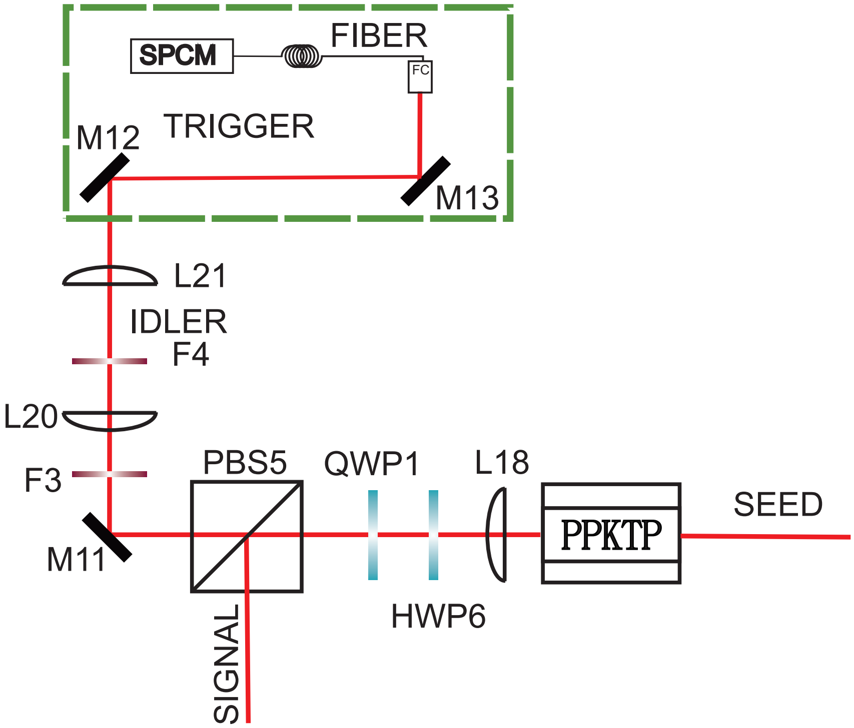

Figure 3.6: Coupling of seed into trigger channel.

of PBS7 and HWP8, we add a lens (L19) to focus the beams into the photodiode detection area - this enhances the efficiency of BHD system because the detection of marginal distribution depends on how the spatial mode of the mixed beams is detected on the sensitive area of the detector.

3.2.7 Final setup

At this point all the components are classically aligned and we need to take the measurements. That requires the blocking of seed (remember, seed is there just for alignment). We uses a computerized acquisition card for analyzing and storing the data (Agilent Acqiris DP211, 2GSamples/s, 250 MHz). The output signal of the HD is weak and hence we used an amplifier (ZFL-500LN).

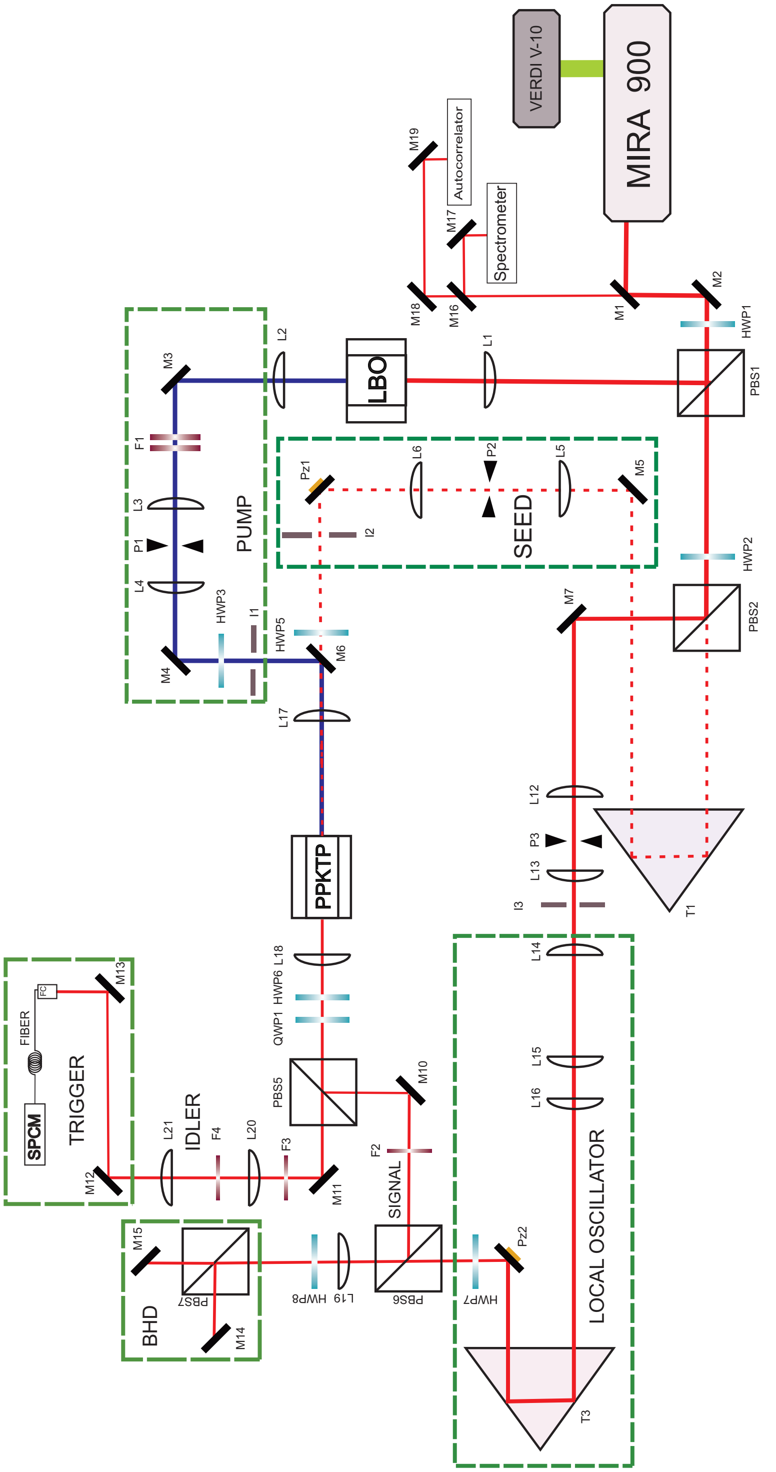

Figure 3.7: Complete experimental set-up for single photon generation.

With the signal channel blocked, the homodyne output corresponds to quadrature fluctuations of the vacuum which can be used to calibrate the detector. The produced distribution is expected to have a Gaussian shape. The acquired quadrature samples can be normalized (by varying both the scale and origin) to show an expectation value of 0 and a standard deviation of $1/\sqrt{2}$.

When the pump and signal channels are opened, the photons in the trigger channel that are coupled to the SPCM generate count events monitored by a frequency counter to give the single-photon preparation rate. We regularly obtain rates in the range of 70-90 kHz. It is important to prevent any stray light influx to the SPCM, as the dark counts lead to an inefficiency (η_{dc}) in homodyne detection. Therefore, the SPCM and fiber are enclosed inside a dark box, and during the experiment all major sources of light switched off. Dark counts $\sim$ 1kHz are usually observed.

The entire set-up is shown in Fig. 3.7.

3.2.8 Detection and measurement

In this section we will deal with light at a quantum level (the alignment procedure was performed with macroscopic amounts of light). The two main devices used for the detection and measurement of the state were the single-photon counter and the HD.

The homodyne detector enables us to gather quadrature ensembles of the quantum state in the signal channel, which is triggered from the SPCM in the idler channel (shown in figure 3.7). A software program captures data segment of length 128 ns each (roughly 9 pulse-periods), centered at the *triggered pulse*. For single-photon Fock state, all but the 5th pulse correspond to vacuum fluctuations. We acquire $N = 10^6$ segments of 9 pulses each. The acquired data split into two files, containing $N\ X\ 8$ vacuum quadrature and N single-photon quadrature samples, respectively. By applying the appropriate rescaling (dependent on the vacuum calibration) to the experimentally obtained values of the variance of the single-photon Fock state, it is possible

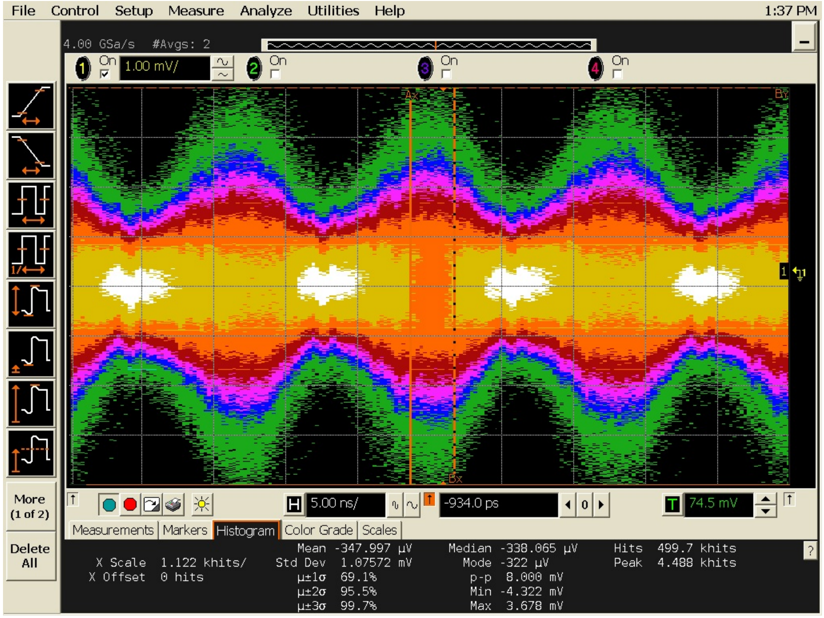

```
                          Mean -347.997 µV     Median -338.065 µV     Hits  499.7 khits
 X Scale  1.122 khits/  Std Dev  1.07572 mV     Mode -322 µV          Peak  4.488 khits
X Offset  0 hits          µ±1σ  69.1%           p-p  8.000 mV
                          µ±2σ  95.5%           Min -4.322 mV
                          µ±3σ  99.7%           Max  3.678 mV
```

Figure 3.8: Pulsed homodyne output. The single photon quadrature information is contained in the middle pulse, which corresponds to a triggered event.

to calculate the overall efficiency of an acquired dataset [20]. With a high photon-production rate and the fast acquisition card, we can thus maximize the overall quantum efficiency η_{eff} of the single-photon Fock state in real time. Once we have a certain η_{eff}, we can maximize this value by improving the signal-LO mode matching by tracking its effect on η_{eff} in real time while performing the experiment.

Following steps can be taken to improve η_{eff} (see figure 3.7):

- The visibility between the signal and LO field can be improved by walking the signal beam with mirror M10 and PBS6 as well as by changing the LO path length with prism T3.
- The fiber coupling can be changed by slight changes on the optical components of the trigger channel.
- Slight change in the orientation and the temperature of the PPKTP crystal can also in-

crease the η_{eff} because of change in the phase-matching conditions, affecting the modes of the signal and trigger fields.

3.2.9 State reconstruction

To reconstruct the quantum state we need marginal distributions acquired for different phases (θ) of the quantum state. Once the phase-quadrature pairs are available, the complete information about the state of the system can be extracted using the maximum-likelihood estimation method (see section 2.5) [31, 41]. In our case, since the single-photon Fock state is insensitive to phase variations, there is no necessity of controlling θ.

Marginal distributions (Quadratures)

We collected thousands of 9 pulse segments (8 vacuum and 1 single photon). By integrating over time intervals inside the pulses the software controlling the acquisition card generates the marginal distributions for vacuum and single photon from the data point distribution inside the selected regions [20]. This homodyne data can be processed to perform state reconstruction of the single-photon Fock state

Density matrix and Wigner function

After processing the data and applying the maximum-likelihood algorithm to it, we obtained the density matrix for the quantum state of the light field measured by the HD, that describes the observed quadratures to the best possible extent. From this density matrix the Wigner function of the state can be subsequently reconstructed. Both the density matrix and the reconstructed Wigner function are shown in Fig. 3.9. Experimental losses such as optical, detector and mode-mismatching lead to the reconstruction of a statistical mixture of the single photon and vacuum. This implies that, the total efficiency obtained for the production and detection of a single photon with this experimental setup was of $\eta_{eff} = 58\%$.

In our reconstruction algorithm we truncated the optical Hilbert space in the Fock basis to

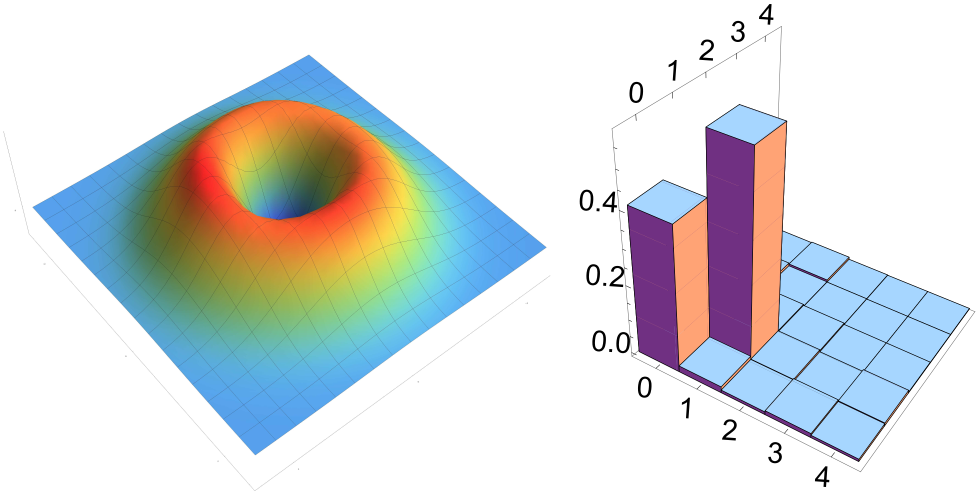

Figure 3.9: (Left) Wigner function. (Right) Density matrix for $\eta_{eff} = 58\%$

a photon number of 4. The numerical value of density matrix elements are: $\rho_{00} = 0.4114$, $\rho_{11} = 0.5800$, $\rho_{22} = 0.0061$, $\rho_{33} = 0.0013$, $\rho_{44} = 0.0012$

Despite the overall efficiency of 58%, we were able to measure a state similar to a single photon Fock state with remarkable non-classical features, in particular the central dip in the reconstructed Wigner function. Now, once we have a characterized our single photon source, we can move on to the QPT.

3.3 Quantum Process Tomography

Following the discussion of section 2.6, we need to experimentally estimate the process tensor of quantum black boxes using Maximum likelihood estimation. In this thesis, we have estimated the tensor for two ”black boxes” (quantum process) - photon addition and subtraction.

3.3.1 Experimental implementation of photon addition

Once we have the single photon source, getting a single photon added coherent state (SPACS) is somewhat straightforward. We just need to have a source of coherent state (probe field) in the same spatio-temporal mode as in the single-photon, which we can get if we would take a portion of light beam from the local oscillator (LO). We have seen before, LO is temporally and spatially mode matched with the single-photon and if we would take a portion of LO as a probe field then we do not have to worry about its mode-matching with the single-photon. The experimental set-up is similar to the one we have for the single-photon experiment in the previous section except for one extra portion in this configuration, where we included a source of coherent state into the PPKTP crystal (shown as blue-dashed block in figure 3.10). Coherent states are simply obtained by splitting off a portion of initial LO using Half-Wave plate (HWP4) and PBS (PBS3). We also have a combination of PBS and LO in the coherent channel (not shown in Fig. 3.10) which enables us to change the amplitude of coherent state entering into the PPKTP crystal.

We used the same primary laser source, a mode-locked Ti:Sa laser emitting ~ 1.7 ps pulses at a repetition rate of 76MHz. Single-photon addition is experimentally implemented in a conditional way, heralded in trigger channel using detector (SPCM, an avalanche photodiode which can discern there being photons from no photons, Fig. 3.10). We have seen in the section 2.3.1 that such a scheme is a very faithful implementation of the ideal singlemode photon addition operator for states with low mean photon numbers. The resulting states are then analyzed by a balanced homodyne apparatus (BHD) working on a pulse-to-pulse basis triggered by the SPCM detectors. The signal state is mixed with a strong reference coherent field (the local oscillator (LO) a portion of the laser output) on a 50:50 beam splitter (PBS6).

Measurement and result

We took the measurement for five different values of α and they are $\alpha = 0$, 0.23, 0.32, 0.61 and 0.87. Table. 3.1 has the elements of density matrices for different alpha values. Even for $\alpha = 0$, we have a mixture of vacuum and single photon because of losses in our experimental set-up (see previous section). Losses are discussed in detail in the next subsection.

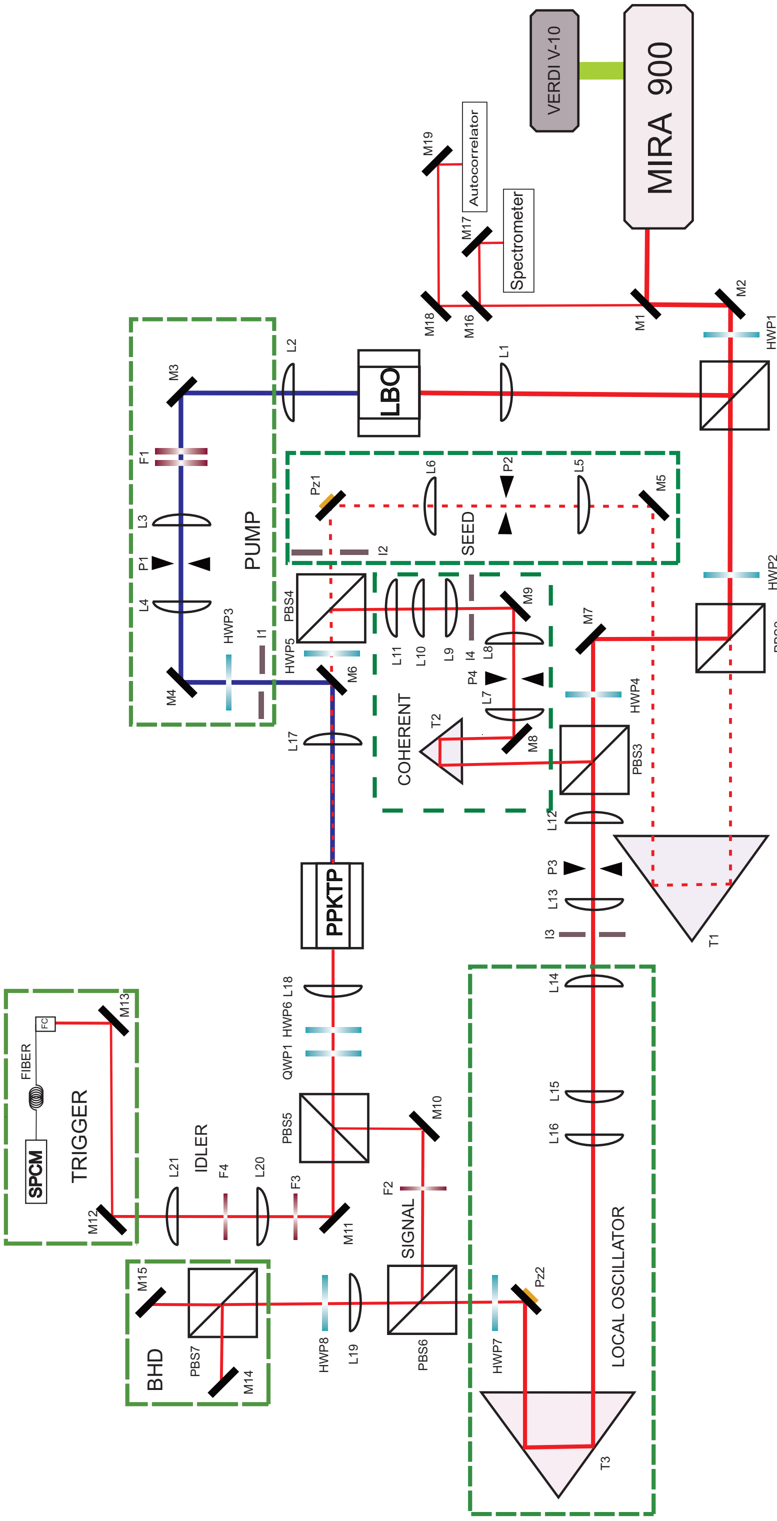

Figure 3.10: Complete layout of experimental set-up for photon addition.

Table 3.1: Density matrix elements for different alpha values, displaced to the origin.

α	ρ_{00}	ρ_{11}	ρ_{01}	ρ_{10}	ρ_{22}
0.0	0.45	0.533	0.006	0.006	0.013
0.23	0.503	0.482	0.185	0.185	0.012
0.32	0.521	0.466	0.245	0.245	0.011
0.61	0.583	0.406	0.286	0.286	0.008
0.87	0.656	0.334	0.318	0.318	0.008

In Fig. 3.11 we can see the different Wigner function for different alpha's and can observe the effect of increasing α, with increasing the value of alpha the dip in the Wigner function decreases and state becomes more classical.

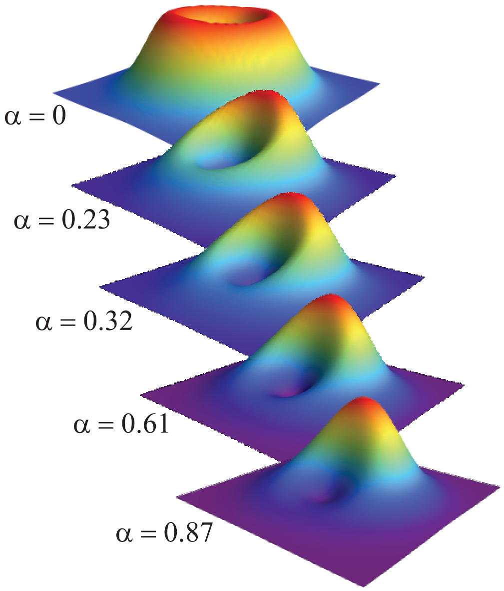

Figure 3.11: The Wigner functions of coherent states of different amplitudes subjected to the photon creation operator; All of them are displaced at the origin.

3.3.2 Experimental implementation of photon subtraction

The idea behind this experiment is similar to photon addition and that implies, we have used a portion of the experiment such as LO, BHD, Trigger channel and coherent state as an input probe state. One major difference is that we did not use down-conversion at all.

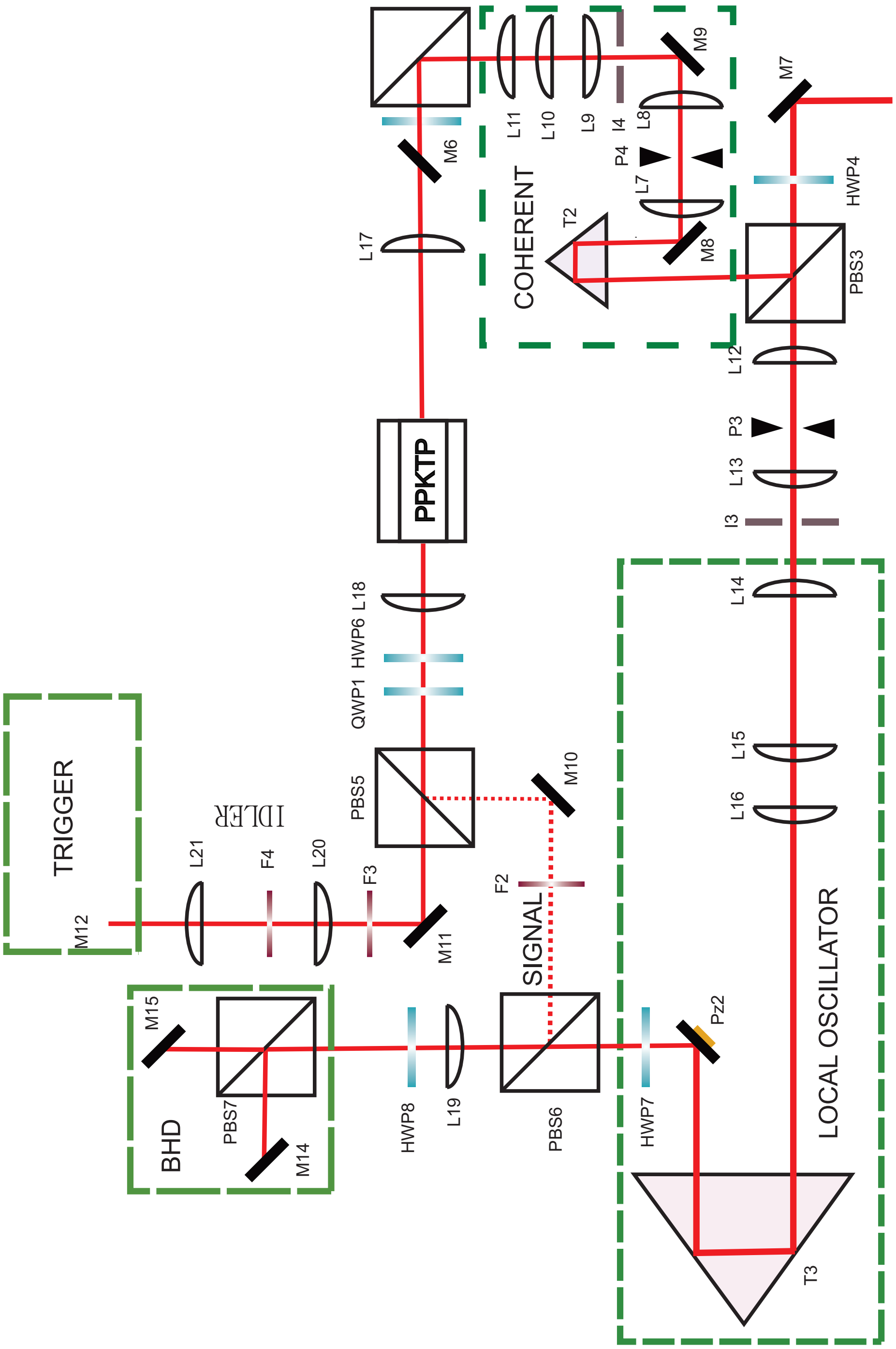

Figure 3.12: Complete layout of experimental set-up for photon subtraction.

We have used the same laser and set-up to maintain the consistency throughout the experiments – a mode-locked Ti:Sa laser emitting $\sim$ 1.7 ps pulses at a repetition rate of 76MHz (Fig. 3.12). Single-photon subtraction is experimentally implemented in a conditional way: a high-transmissivity BS is placed in the path of the light field and the quantum operation succeeds each time that an on/off detector (SPCM, an avalanche photodiode which can discern there being photons from no photons) fires in the reflected mode (Fig. 3.12). We have discussed in section 2.3 that such a scheme is a very faithful implementation of the ideal single-mode photon annihilation operator for states with low mean photon numbers and for low BS reflectivity [5]. The resulting states are then analyzed by a balanced homodyne apparatus (BHD) working on a pulse-to-pulse basis triggered by the SPCM detectors. The signal state is mixed with a strong reference coherent field (the local oscillator (LO) a portion of the laser output) on a 50:50 beam splitter (PBS6).

Coherent states are simply obtained by splitting off a portion of initial LO using Half-Wave plate (HWP4) and PBS (PBS3). We employed the similar method of BHD to gather the

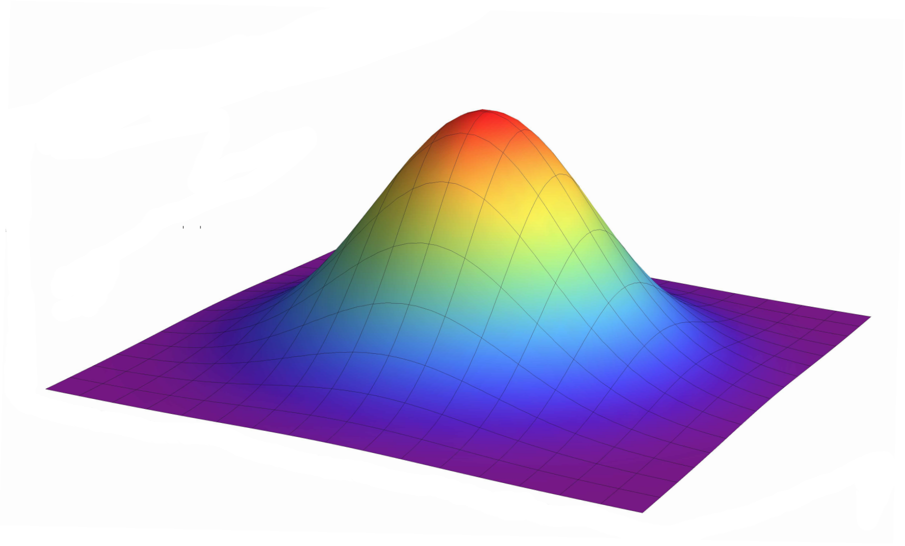

Figure 3.13: Wigner function of the output state for arbitrary α

quadrature values of the output state for different values of α. However, unlike single photon or SPACS case, photons in the signal and idler channel are not correlated. In other words, irrespective of value of α for the input states, the quadrature statistics of output states will look like a vacuum states (which is just a displaced coherent state). Fig. 3.13 is the Wigner function for an arbitrary α. This proves, $\hat{a}$ is an eigen state of $|\alpha\rangle$.

3.3.3 QPT results

The processes we study are non-deterministic, and their probability of occurrence depends on the input state. Accounting for this dependence is crucial for the correct reconstruction. In csQPT, this is done by renormalizing the process output for the probe states so that $\mathrm{Tr}[\mathcal{E}(|\alpha\rangle\langle\alpha|)]$ in Eqs. (2.99 and (2.100) is proportional to the probability of the heralding event [8]. To illustrate the role of this step, let us review Eq. (2.99 for the photon annihilation operator, such that $\mathcal{E}(|\alpha\rangle\langle\alpha|) = |\alpha|^2 |\alpha\rangle\langle\alpha|$. If the coefficient $|\alpha|^2$, responsible for the non-deterministic nature of $\hat{a}$, is neglected, we would obtain the identity process. We see, remarkably, that the "lowering" feature of $\hat{a}$ arises in csQPT entirely due to the variation of the event probability as a function of the probe amplitude, rather than transformation of the probe state itself.

The information on the heralding event probability is obtained by keeping track of the photon count rates for various input states. Theoretically, we expect these rates to behave as

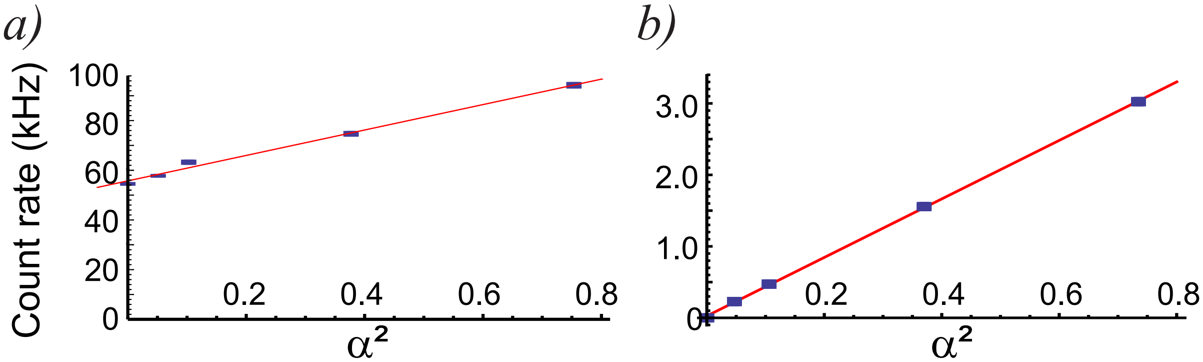

Figure 3.14: Event count rate for the photon creation (a) and annihilation (b) operators as a function of the input coherent state amplitudes. Fits are according to $A\alpha^2$ and $B(1+\alpha^2)$, respectively, with A and B being the fitting parameters.

(see section 2.3.1 and 2.3.2)

$$\mathrm{pr}_{\hat{a}}(\alpha) \propto \langle\alpha|\hat{a}^{\dagger}\hat{a}\,|\alpha\rangle = \alpha^2; \quad \mathrm{pr}_{\hat{a}^{\dagger}}(\alpha) \propto \langle\alpha|\hat{a}\hat{a}^{\dagger}\,|\alpha\rangle = 1 + \alpha^2. \tag{3.2}$$

The experimentally observed dependencies are displayed in Fig. 3.14. Fitting the horizontal scale of the plot of the count rate for the photon creation operator allows us to calibrate the amplitudes of the probe coherent states (next section).

3.3.4 Amplitude calibration of coherent state

The experiment involves coherent states of extremely weak amplitudes. These states are generated by a series of variable attenuators, each made up of a half-wave plate and a polarizer. While ratios of these amplitudes are precisely determined by the orientations of these wave plates, evaluating their common scale factor is a challenge. In homodyne tomography experiments, a convenient gauge is provided by the quadrature variance of the vacuum state. By comparing the phase-dependent quadrature noise statistics with this variance, one evaluates the amplitude. In the present experiment, it is not possible for the following reason.

Due to imperfect subtraction of photocurrents in homodyne detector, the output electronic signal of the broadband balanced detector used in this experiment features a strong, fluctuating component at the repetition frequency of the master laser pulses [39]. This component had to be suppressed by means of notch filtering. As a result, all quadrature measurements associated with a heralding event become displaced by the average quadrature value of the neighboring unheralded pulses.

This displacement must be accounted for when processing the data. Because the probabilities of the photon creation and annihilation events in our setup are relatively low, we can assume that the state propagating through the black box when the single-photon counter does not ”click” does not get modified. Accordingly, the unheralded events correspond to coherent states that have undergone transformations with the identity process in place of the photon creation and annihilation ”black boxes”. The amplitudes and mean quadratures of these coherent states are readily calculated from the amplitude of the coherent state $|\alpha\rangle$ at the process input. This latter amplitude is, in turn, evaluated by fitting the photon creation event rate as a function of the target coherent state amplitude. We know the count rate should be proportional to $(1+\alpha^2)$ (from (3.2)), so once we know the relative count rates we can calibrate the α values associated using $(1+\alpha^2)$.

We can also calibrate the alpha values from the states itself. For example, we know the theoretical dependence of density matrix elements on alpha and this dependence can be fitted with the experimentally obtained density matrix elements (shown in figure 3.15 and 3.16).

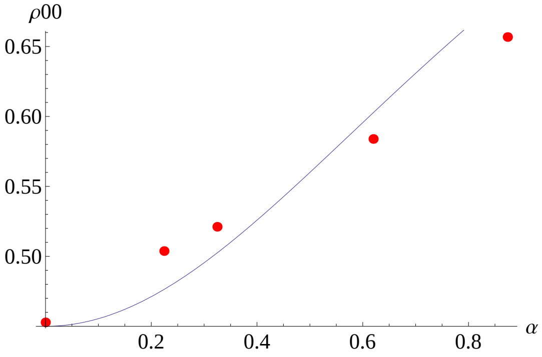

Figure 3.15: Theoretical dependence of ρ_{00} element of density matrices for photon added states on alpha fitted with the experimentally obtained ρ_{00} elements density matrix.

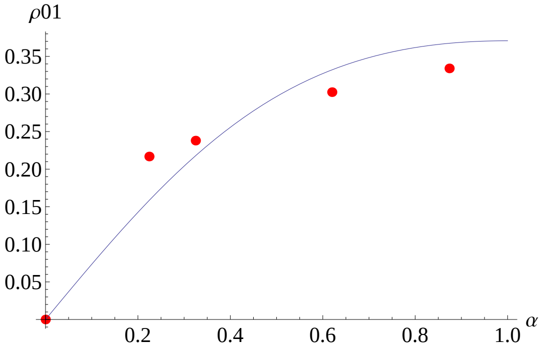

Figure 3.16: Theoretical dependence of ρ_{01} element of density matrices for photon added states on alpha fitted with the experimentally obtained ρ_{01} elements density matrix.

Process tensor

The diagonal elements $\mathcal{E}_{kk}^{mm}$ of the reconstructed process tensors are shown in Fig. 3.18 and 3.19. These elements permit straightforward interpretation: they give the probability that the output of the quantum ”black box” contains k photons when the m-photon state is present at the input. According to Eq. (1.1), we expect $(\mathcal{E}_{\hat{a}})_{kk}^{mm} = m\delta_{k,m-1}$ and $(\mathcal{E}_{\hat{a}})_{kk}^{mm} = (m+1)\delta_{k,m+1}$. The experimental result is consistent with this expectation and explicitly features the ”raising” and ”lowering” properties of $\hat{a}^\dagger$ and $\hat{a}$. For input state $|m\rangle$, the output state is similar to $|m+1\rangle$ for operator $\hat{a}^\dagger$ and $|m-1\rangle$ for operator $\hat{a}$. The height of the bars in the plots increases linearly with m, which is associated with the squared factors $\sqrt{m+1}$ and $\sqrt{m}$ in the right-hand sides of Eq. (1.1). The imperfections visible in the evaluated tensors are likely due to the oversimplified modeling of the experiment in the process reconstruction.

Experimental imperfections

The models used to account for the experimental imperfections are shown in Fig. 3.17. For the process associated with operator $\hat{a}$, the detrimental effects are the linear losses, non-unitary quantum efficiencies of the homodyne detector photodiodes, electronic noise of the homodyne detector [38] and mode-mismatch between the process output mode and the local oscillator. All these effects can be modeled by an attenuator with transmission $\eta_1 = 0.72$ placed after an ”black box” containing an ideal photon annihilation operator [Fig. 3.17(a)]. Accounting for linear losses in maximum-likelihood homodyne reconstruction is a well-known technique, which consists of modifying the measurement operator associated with detecting field quadrature values [7, 41, 9] (discussed before).

For the photon creation, accounting for the imperfections is more complicated, because one needs to take into account mode mismatch between the signal mode of parametric down-conversion and that of the probe field. Accordingly, the model consists of a Mach-Zehnder interferometer, and an ideal photon creation operator is placed into one of its arms [Fig. 3.17(b)].

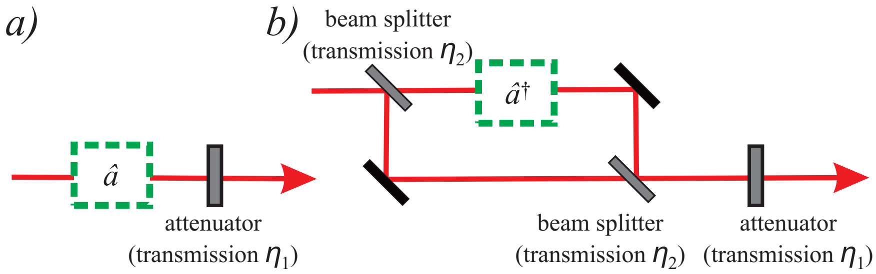

Figure 3.17: Model of experimental imperfections for the photon annihilation (a) and creation (b) setups.

The interferometer is aligned for constructive interference in one of the outputs. The splitting ratio of the interferometer can be determined by analyzing the reconstructed process output when the probe is in the vacuum state. With a high precision, it is a statistical mixture of the single-photon and vacuum states [20], with the single-photon fraction equal to $\eta_1\eta_2 = 0.55$. Knowing that $\eta_1 = 0.72$, we conclude that $\eta_2 = 0.76$.

With this model, if the coherent state entering the interferometer is $|\alpha_{\text{init}}\rangle$, the state entering the ”black box” is $|\alpha\rangle = \left|\sqrt{\eta_2}\alpha_{\text{init}}\right\rangle$. The output of the ”black box” undergoes transformation that is equivalent to a linear loss channel with transmissivity $\eta_1\eta_2$ followed by phase-space displacement by $\Delta X = \sqrt{2\eta_1}(1-\eta_2)\alpha_{\text{init}}$. While the linear loss can be accounted for by the iterative algorithm, the displacement must be undone by modifying the measured quadrature data. Specifically, we subtract $\Delta X\cos\theta$ from each experimentally measured sample of quadrature observable $\hat{X}_\theta = \hat{X}\cos\theta + \hat{P}\sin\theta$, where θ is the local oscillator phase. The modified values are then used as input for the iterative algorithm.

Photon addition

We implemented the csQPT on Photon addition for five different set of α values (0, 0.23, 0.32, 0.61, 0.87). For each input probe state, the output state dataset consisted of 100,000 *quadratures* and *phases* point X, θ. This set of data was subjected to the reconstruction method using Eq. 2.103. We observed a combination of losses (mode-mismatch, optical and detector loss) with $\eta_{loss_{effective}} = 0.45$.

The result obtained by running the reconstruction technique is a 4-dimensional process tensor whose diagonal elements have a simple interpretation. The diagonal element $\mathcal{E}_{kk}^{mm}$ denotes the probability that the output contains k photons when the process is subjected to m input photons as shown in the Fig. 3.18. Fig. 3.18 also includes the diagonal elements of the theoretically reconstructed process tensor and it exhibits a close match with the experimental reconstructed process.

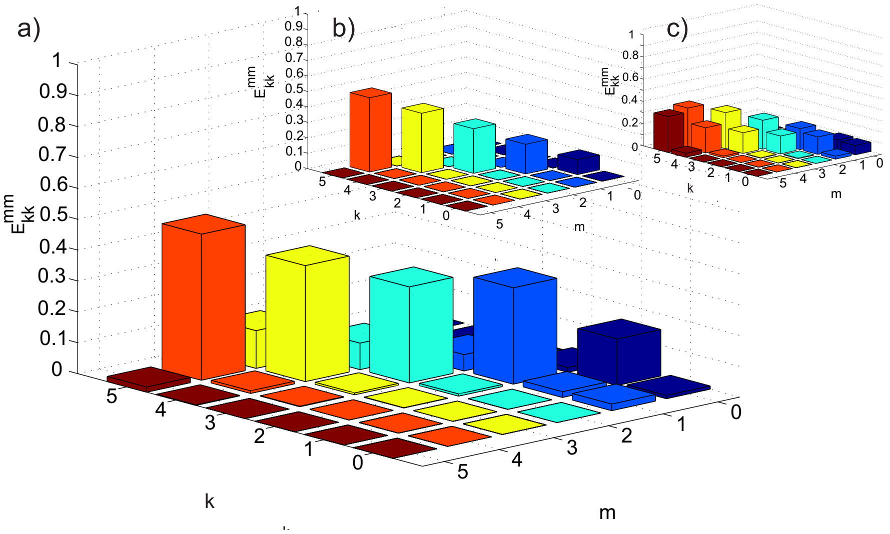

Figure 3.18: The "diagonal" value of superoperator $\mathcal{E}_{kk}^{mm}$ for Photon addition. (a) From experimental data with correction for losses. (b) From monte-carlo simulated data without any loss [9]. (c) From experimental data without correction for loss. Each color corresponds to the photon number distribution in the output state for the Fock state $|m\rangle$ at the input.

Photon subtraction

We implemented the csQPT on Photon addition for five different set of α values (0, 0.22, 0.33, 0.61, 0.86). For each input probe state, the output state dataset consisted of 100,000 *quadratures* and *phases* point X, θ. This set of data was subjected to the reconstruction method using Eq. 2.103. We observed an optical and detector loss of 28%.

The result obtained by running the reconstruction technique is a 4-dimensional process tensor whose diagonal elements have a simple interpretation. The diagonal element $\mathcal{E}_{kk}^{mm}$ denotes the probability that the output contains k photons when the process is subjected to m input photons as shown in the Fig. 3.19. Fig. 3.19 also includes the diagonal elements of the theoretically reconstructed process tensor and it exhibits a close match with the experimental reconstructed process.

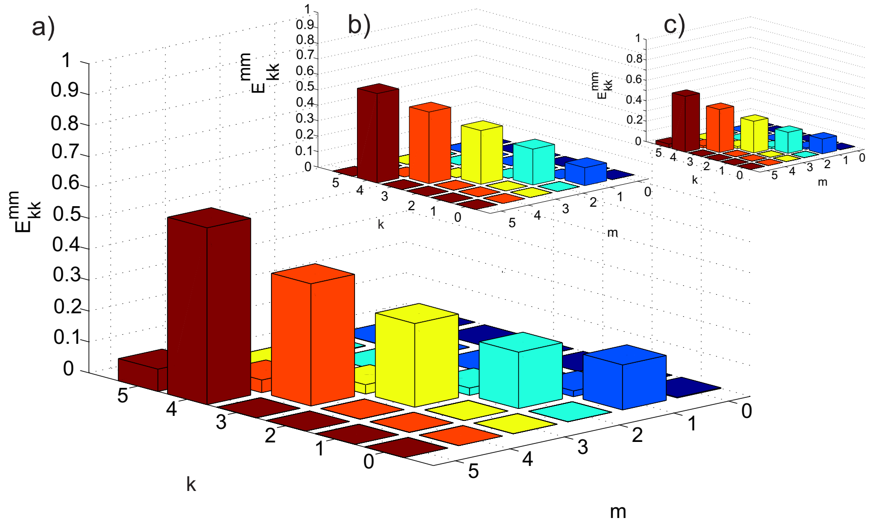

Figure 3.19: The "diagonal" value of superoperator $\mathcal{E}_{kk}^{mm}$ for Photon subtraction. (a) From experimental data with correction for losses. (b) From monte-carlo simulated data without any loss [9]. (c) From experimental data without correction for loss. Each color corresponds to the photon number distribution in the output state for the Fock state $|m\rangle$ at the input.

Performance test

The consistency of the estimated process tensors with those theoretically expected can be quantified using the fidelity benchmark. Figure 3.20 shows the worst-case fidelities between normalized states $\mathcal{E}_{\hat{a},\hat{a}^\dagger}(|\psi\rangle\langle\psi|)$ and $\hat{a}, \hat{a}^\dagger |\psi\rangle$ of the reconstructed processes $\mathcal{E}_{\hat{a},\hat{a}^\dagger}(|\psi\rangle\langle\psi|)$ of photon annihilation and creation, respectively (see equation (3.3))[52]. The fidelity is evaluated for the processes applied to pure quantum states within subspaces of the optical Hilbert space ($\mathcal{H}$)

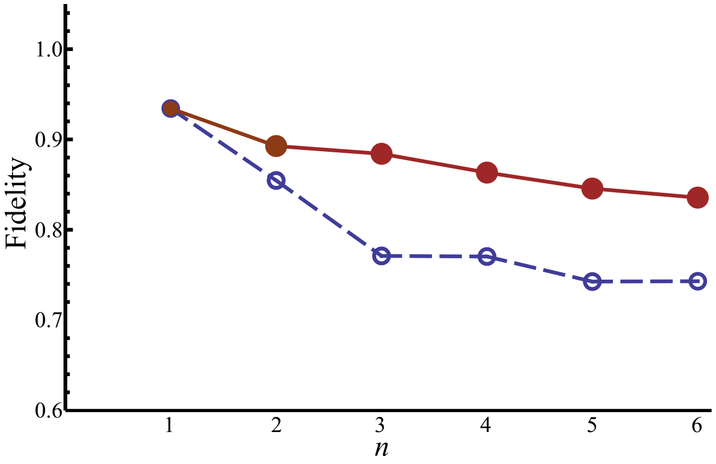

Figure 3.20: Worst-case fidelities for the photon annihilation (solid line) and creation (dashed line) processes acting within subspaces $\mathcal{H}(n)$ of the optical Hilbert space.

spanned by number states $|1\rangle \ldots |n\rangle$ and $|0\rangle \ldots |n-1\rangle$, respectively, with n ranging between 1 and the number of photons in the reconstructed tensor, $n_{\max} = 6$. The fidelities decrease with increasing n because for high photon-number states, the overlap with the probe states is low and hence the experimental data does not provide sufficient information about the effect of the process on these states [9]. The worst-case fidelity is defined as

$$\mathcal{F}_{\hat{a}^\dagger} = \min_{\psi \,\in\, \mathcal{H}(0,\, n_{\max}-1)} \langle \psi_{th} |\, \mathcal{E}_{\hat{a}^\dagger}(|\psi\rangle\langle\psi|)\, |\psi_{th}\rangle; \tag{3.3}$$

$$\mathcal{F}_{\hat{a}} = \min_{\psi \,\in\, \mathcal{H}(1,\, n_{\max})} \langle \psi_{th} |\, \mathcal{E}_{\hat{a}}(|\psi\rangle\langle\psi|)\, |\psi_{th}\rangle. \tag{3.4}$$

In order to find the worst-case, we minimized over $\mathcal{H}(0,\ n_{\max}-1)$ for photon creation and $\mathcal{H}(1,\ n_{\max})$ for photon annihilation through a Monte-Carlo simulation, which involved introducing small random changes in $|\psi\rangle$ and accepting the change whenever the value of the fidelity decreases.

Chapter 4

Summary and Future Possibilities

In this thesis, we have demonstrated an experimental implementation of quantum process tomography for photon addition and subtraction operator. Since these two processes are trace non-preserving operators, we have approximated their implementation in the framework of deterministic Hamiltonian evolution of a physical system. Implying, the action of operators occurs with probability less than one, but is heralded by a classical event. Implementation of photon addition was more challenging because it required to have a reliable and efficient single photon source, where we used a conditionally prepared single photon source with an average fidelity of 55%.

The combination of a high preparation rate, a fast acquisition system both in counting photons and measuring signal-quadratures samples in time domain permitted an improvement of overall efficiency of the process. An elaborate scheme to analyze the black box by probing them with coherent states (weak laser pulses) of different amplitude and measuring quantum fluctuation of the output electromagnetic field was implemented. Using the experimentally obtained process tensor, we can now predict the effect of black box for any arbitrary state of light within a practically relevant subspace of the optical Hilbert space. The reconstructed process tensors exhibit ”raising” and ”lowering” properties of these operations - this is first experimental implementation in which complete tomography of trace-non-preserving quantum processes has been carried out.

With the implementation of QPT for photon addition and subtraction operators, we have achieved an important milestone in the fundamental quantum optics - these operators effectively define today’s quantum optics as we know it. This idea behind this work can be extended to other physical processes such as quantum process tomography of controlled-NOT gate [53] and characterization of quantum memory.

Bibliography

[1] P. A. M. Dirac, Proc. R. Soc. Lond. A 114, 243-265 (1927).

[2] A. Zavatta, S. Viciani, and M. Bellini, Phys. Rev. A 72, 023820 (2005).

[3] A. Ourjoumtsev, R. Tualle-Brouri, J. Laurat and P. Grangier, Science 312 83 (2006).

[4] J. S. Neergaard-Nielsen *et al.,* Phys. Rev. Lett. 105, 053602 (2010).

[5] V. Parigi, A. Zavatta, M. S. Kim and M. Bellini, Science 317, 1890-1893 (2007).

[6] M. Lobino *et al.*, Science 332, 563 (2008).

[7] U. Leonhardt, Measuring the Quantum state of Light, Cambridge University Press (1997).

[8] S. Rahimi-Keshari *et al.*, New J. Phys. 13, 013006 (2011).

[9] A. Anis and A. I. Lvovsky, arXiv:1204.5936v1 (2012).

[10] Bo Thide, ”Electromagnetic Field Theory”, (Upsilon books, Sweden, 2004).

[11] E. P. Wigner, Phys. Rev. 40, 749759 (1932).

[12] A. Yariv, ”Quantum Electronics”, 3rd ed., p. 400 (John Wiley Sons, 1989, USA).

[13] R. W. Boyd, ”Nonlinear Optics”, (Academic Press, 1992, USA).

[14] C. K. Hong and L. Mandel, Phys. Rev. Lett., 56:58-60, (Jan 1986).

[15] D. Bouwmeester, A. Ekert and A. Zeilinger, The Physics of Quantum Information, (Springer, Berlin, 2000).

[16] T. E. Keller and M. H. Rubin, Phys. Rev. A 56, 1534 (1997).

[17] W. P. Grice and I. A. Walmsley, Phys. Rev. A 56, 1627 (1997).

[18] T. Aichele, A. I. Lvovsky and S. Schiller. Eur. Phys. J. D 18, 237 (2002).

[19] G. S. Agarwal and K. Tara, Phys. Rev. A 43, 492 (1991).

[20] S. R. Huismann *et al.,* , Opt. Lett. 34, 18 (2009).

[21] J. Wenger, R. Tualle-Brouri and P. Grangier Phys. Rev. Lett. 92 153601 (2004).

[22] M. S. Kim, E. Park, P. L. Knight and H. Jeong Phys. Rev. A 71 043805 (2005).

[23] T. Opatrny, G. Kurizki and D-G. Welsch Phys. Rev. A 61 032302 (2000).

[24] N. J. Cerf, O. Kruger, P. Navez, R. F. Werner and M. M. Wolf Phys. Rev. Lett. 95 070501 (2005).

[25] J. Eisert, S. Scheel and M. B. Plenio Phys. Rev. Lett. 89 137903 (2002).

[26] G. Giedke and C. J. Ignacio Phys. Rev. A 66 032316 (2002).

[27] I. Jex, S. Stenholm, A. Zeilinger, Opt. Comm. 117, 95-101 (1995).

[28] H. P. Yuen and J. H. Shapiro, L. Mandel and E. Wolf [eds.], Coherence and Quantum Optics IV (Platinum, New York, 1978).

[29] D. F. Walls and C. J. Milburn, ”Quantum Optics” Springer-Verlag, Berlin Heidelberg (1994).

[30] J. H. Shapiro, H. P. Yuen, J. A. Machado Mata, IEEE Trans. Inf Theory IT-25, 179 (1979).

[31] A. I. Lvovsky and M. G. Raymer, Rev. Mod. Phys. 81, 299 (2009).

[32] H. P. Yuen and V. W. S. Chan, Opt. Lett., 8, 177. (1983).

[33] E. Barrios. ”Design and Characterization of Wideband Balanced Homodyne Detectors for Quantum Homodyne Tomography”, MSc thesis, University of Calgary (2012).

[34] H. Hansen. Generation and characterization of new quantum states of the light field, Ph.D. Thesis, University of Konstanz (2000).

[35] S. Babichev. Quantum optical technology at the single photon level Ph.D Thesis. University of Calgary (2006).

[36] F. Grosshans and P. Grangier. Eur. Phys. J. D 14, 119-125 (2001).

[37] J. H. Shapiro. IEEE J. Quant. Elec. QE-21. No.3. March 1985.

[38] J. Appel, D. Hoffman, E. Figueroa and A. I. Lvovsky. Phys. Rev. A 75, 035802 (2007).

[39] R. Kumar, E. Barrios, A. MacRae, E. Cairns, E. H. Huntington and A. I. Lvovsky, arXiv.org:1111.4012 (2011).

[40] H. A. Bachor and T. C. Ralph. A guide to experiments in quantum optics. Wiley-VCH, 2nd ed. (2009).

[41] A. I. Lvovsky, J. Opt. B 6, S556 (2004).

[42] M. Jezek, J. Fiurasek, and Z. Hradil Phys. Rev. A 68 012305 (2003).

[43] J. Fiurášek and Z. Hradil Phys. Rev. A 63 020101(R) (2001).

[44] Z. Hradil, J. Řeháček, J. Fiurášek, and M. Ježek Maximum-Likelihood Methods in Quantum Mechanics in *Quantum State Estimation* (*Springer Lecture Notes in Physics*), ed M G A Paris and J. Řeháček (2004).

[45] A. I. Lvovsky, H. Hansen, T. Aichele, Phys. Rev. Lett. 87, 050402 (2001).

[46] K. Vogel, and H. Risken, Physical Review A 40, 2847 (1989).

[47] M. Sasaki, and S. Suzuki, Physical Review A 73, 043807 (2006).

[48] R. W. Boyd, Nonlinear Optics, Second Ed. Academic Press. (2003).

[49] S. Babichev. Quantum optical technology at the single photon level Ph.D Thesis. University of Calgary (2006).

[50] N. Jain. Quantum optical state engineering at the few-photon level, MSc thesis, University of Calgary (2009).

[51] J. Řeháček, Z. Hradil, E. Knill, and A. I. Lvovsky, Phys.Rev. A 75, 042108 (2007).

[52] A. I. Lvovsky, B. C. Sanders, and W. Tittel Nature Photonics 3 706-14 (2009).

[53] J. L. O'Brien *et al.,* , Phys. Rev. Lett. 93, 080502 (2004).